ChemComm

FEATURE ARTICLE

View Article Online
View Journal | View Issue

Check for updates

Cite this: *Chem. Commun.*, 2024, **60**, 12118

Advances and challenges in designing active site environments in zeolites for Brønsted acid catalysis

Sopuruchukwu Ezenwa and Rajamani Gounder *

Zeolites contain proton active sites in diverse void environments that stabilize the reactive intermediates and transition states formed in converting hydrocarbons and oxygenates to chemicals and energy carriers. The catalytic diversity that exists among active sites in voids of varying sizes and shapes, even within a given zeolite topology, has motivated research efforts to position and quantify active sites within distinct voids (synthesis–structure) and to link active site environment to catalytic behavior (structure–reactivity). This Feature Article describes advances and challenges in controlling the position of framework Al centers and associated protons within distinct voids during zeolite synthesis or post-synthetic modification, in identifying and quantifying distinct active site environments using characterization techniques, and in determining the influence of active site environments on catalysis. During zeolite synthesis, organic structure directing agents (SDAs) influence Al substitution at distinct lattice positions *via* intermolecular interactions (*e.g.*, electrostatics, hydrogen bonding) that depend on the size, structure, and charge distribution of organic SDAs and their mobility when confined within zeolitic voids. Complementary post-synthetic strategies to alter intrapore active site distributions include the selective removal of protons by differently-sized titrants or unreactive organic residues and the selective exchange of framework heteroatoms of different reactivities, but remain limited to certain zeolite frameworks. The ability to identify and quantify active sites within distinct intrapore environments depends on the resolution with which a given characterization technique can distinguish Al T-site positions or proton environments in a given zeolite framework. For proton sites in external unconfined environments, various (post-)synthetic strategies exist to control their amounts, with quantitative methods to distinguish them from internal sites that largely depend on using stoichiometric or catalytic probes that only interact with external sites. Protons in different environments influence reactivity by preferentially stabilizing larger transition states over smaller precursor states and influence selectivity by preferentially stabilizing or destabilizing competing transition states of varying sizes that share a common precursor state. We highlight opportunities to address challenges encountered in the design of active site environments in zeolites by closely integrating precise (post-)synthetic methods, validated characterization techniques, well-defined kinetic probes, and properly calibrated theoretical models. Further advances in understanding the molecular details that underlie synthesis–structure–reactivity relationships for active site environments in zeolite catalysis can accelerate the predictive design of tailored zeolites for desired catalytic transformations.

Received 12th September 2024,
Accepted 20th September 2024

DOI: 10.1039/d4cc04728a

rsc.li/chemcomm

Open Access Article. Published on 20 September 2024. Downloaded on 1/24/2026 9:35:52 AM.
This article is licensed under a Creative Commons Attribution-NonCommercial 3.0 Unported Licence.

1. Introduction

Zeolites catalyze a wide range of reactions involved in upgrading hydrocarbons and oxygenates to valuable chemicals and energy carriers.[1–4] The substitution of tetrahedrally-coordinated Si^{4+} in the charge-neutral silica framework ($[SiO_{4/2}]$) with Al^{3+} generates anionic centers ($[AlO_{4/2}]^-$), which charge-compensate protons (H^+) that serve as active sites.[5] The pioneering work of Haag and co-workers demonstrated that the rates (per g zeolite) of a series of catalytic reactions including *n*-hexane cracking (811 K) were strictly proportional to the Al content (per g zeolite) among MFI zeolites (Si/Al = 15–100 000).[5,6] Their results suggested either similar reactivity among all 26 possible H^+ sites associated with the 12 crystallographic distinct $[AlO_{4/2}]^-$ positions in the MFI lattice, or a similar distribution of H^+ sites of different reactivity across MFI zeolites synthesized in a similar manner.[5,6] Furthermore,

Davidson School of Chemical Engineering, Purdue University, West Lafayette, IN, 47907, USA. E-mail: rgounder@purdue.edu

 This journal is © The Royal Society of Chemistry 2024

Open Access Article. Published on 20 September 2024. Downloaded on 1/24/2026 9:35:52 AM. This article is licensed under a Creative Commons Attribution-NonCommercial 3.0 Unported Licence.

isolated Brønsted acid sites in microporous and mesoporous aluminosilicates of diverse topologies have similar acid strength, as rigorously quantified by the deprotonation energy (DPE), or the energy required to remove a proton from the conjugate base ($[AlO_{4/2}]^-$) to non-interacting distances.[7–10] However, catalytic diversity exists among varying zeolite topologies and even among samples of a given topology but different synthetic history, as evidenced by variations in site-normalized turnover rates, product selectivity, or deactivation behavior during acid-catalyzed reactions (*e.g.*, alkane cracking[11–14] and dehydrogenation,[11,15] alkene oligomerization[16–19] and hydrogenation,[20] alkanol dehydration,[21–24] alkanol to hydrocarbons,[25–27] aromatic alkylation,[28–31] alkanal–alkene coupling[32,33]).

Classical concepts of shape selectivity[34–37] were historically used to describe how micropores of varying size and connectivity regulate reactant access to active sites (reactant shape selectivity), control product egress from crystallites (product shape selectivity) and restrict formation of certain transition states (transition-state shape selectivity). Yet, in certain cases where reactivity is not controlled by molecular transport within micropores, these heuristic concepts are limited in explaining catalytic differences among zeolite frameworks possessing similarly sized micropore apertures or in a given zeolite framework containing protons in differently sized voids.[38,39] Instead, kinetically controlled reactivity differences during Brønsted acid catalysis are underpinned by the (de)stabilization of reactive intermediates and transition states by electrostatic interactions that depend on the acid strength of the binding site ($[AlO_{4/2}]^-H^+$) and by van der Waals interactions that depend on the size and shape of the confining void.[38–45] Beyond influences of the binding site and the confining void environment, certain rigid arrangements of proximal anionic Al centers also stabilize cationic intermediates and transition states, conferring additional catalytic diversity to zeolite samples of a fixed framework type, even those such as chabazite (CHA) that contain a single crystallographically unique tetrahedral site (T-site) and similar composition (*i.e.*, Si/Al ratio).[13,22,23] Thus, catalytic diversity emanates from variations in the location and arrangement of H^+ associated with the siting of framework Al centers at symmetry-distinct T-sites within varying internal (or intracrystalline) micropores of different shapes and sizes (0.4–1.5 nm diameter), at external (or extracrystalline) surfaces and mesoporous environments (>2 nm diameter) (Fig. 1), or in different lattice arrangements.[46,47] Furthermore, the void environment and arrangement of Al in zeolites affect the location, speciation, and structure of extra-framework metal cations (M^{n+}) and complexes (*e.g.*, $[M_xO_y]^{n+}$) that are active-site precursors or active sites for metal-catalyzed chemistries (*e.g.*, methane partial oxidation on Cu- and Fe-zeolites[48–50] and dehydroaromatization on Mo-zeolites,[51–53] alkane dehydrogenation and dehydroaromatization on Ga- and Zn-zeolites,[54–56] alkene dimerization and oligomerization on Ni-zeolites,[57,58] and reduction and oxidation of nitrogen oxides on Cu-zeolites[59,60]).

As highlighted by various reviews and perspectives over the past decade, designing Brønsted acid zeolites for targeted catalytic applications requires strategies to tailor bulk crystallite properties (*e.g.*, crystallite size and morphology, active site density) that influence the intracrystalline diffusion of molecules[61–78] and approaches to tailor active site properties (*e.g.*, void environments, local arrangements) that influence the stabilities of reactive intermediates and kinetically relevant transition states.[39,46,47,79–87] However, for active site design approaches, challenges in controlling the location of active sites within distinct void environments and in distinguishing

Sopuruchukwu Ezenwa

Sopuruchukwu obtained his BS in Chemical Engineering from Tufts University in 2018 and his PhD in Chemical Engineering from Purdue University in 2024 under the mentorship of Prof. Gounder where he investigated the catalytic consequences of active site environments in Brønsted acid aluminosilicates on aromatic alkylation reactions. His research has been recognized by the ChE Faculty Lectureship Award from Purdue (2024), the Richard J. Kokes award from North American Catalysis Society (2022), and the Catalysis and Reaction Engineering Division Travel Award from AIChE (2022). His research interests center on developing molecular-level insights that enable the design of heterogeneous catalysts and chemical processes for producing chemicals and energy carriers from conventional and emerging feedstocks.

Rajamani Gounder

Rajamani Gounder is the R. Norris and Eleanor Shreve Professor at the Davidson School of Chemical Engineering at Purdue University. He leads a research group that is recognized for studying the kinetic and mechanistic details of catalytic reactions, for synthesizing and designing zeolites and porous materials with tailored site and surface properties, and for developing methods to characterize and titrate active sites in catalytic surfaces. His group studies the fundamental science of catalysis, and its practical applications to help protect our environment and to develop sustainable, lower-carbon footprint routes to synthesize chemicals and fuels needed for society.

Open Access Article. Published on 20 September 2024. Downloaded on 1/24/2026 9:35:52 AM.
This article is licensed under a Creative Commons Attribution-NonCommercial 3.0 Unported Licence.

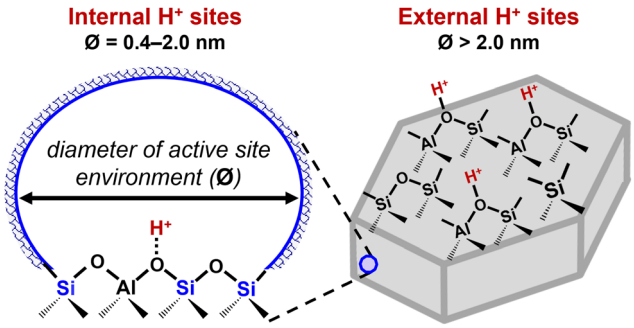

Fig. 1 Scheme showing H^+ sites in internal micropore environments of varying sizes (0.4–2.0 nm diameter) or at external surfaces and mesoporous environments (>2 nm diameter) of Brønsted acid zeolites.

their number and intrinsic reactivity limit the ability to tailor zeolites for desired catalytic transformations. This Feature Article focuses on advances and challenges in developing fundamental synthesis–structure–reactivity relationships for Al (and H^+) siting within internal confining micropores of varying sizes and shapes and at external unconfined surfaces. We exclude discussions on synthesis–structure–reactivity relationships for Al proximity and arrangement, as our perspective on those topics can be found in a previous publication.[47] We also exclude discussions on synthesis–structure–function relationships for bulk crystallite properties that control intracrystalline diffusion phenomena in zeolites.

In Section 2, we connect advances in elucidating the intermolecular interactions that govern the synthetic placement of active sites in distinct internal void environments and highlight complementary approaches to post-synthetically remove acid sites from distinct voids. We also discuss the merits and limitations of characterization techniques often used to assess differences in framework Al siting or H^+ void environments. We further describe catalytic insights from selected case studies that delineate how the active site environment alters kinetically controlled reactivity and selectivity for a given zeolite framework with fixed active site density but varying (post-)synthetic origin. In Section 3, we examine (post-)synthetic strategies and characterization techniques to respectively manipulate and quantify the number of active sites at external unconfined environments. We emphasize that, in this focused perspective, the selected examples from previously published works from our group and the broader literature within the past two decades are chosen to illustrate fundamental insights and elucidate molecular-level details underlying synthesis–structure–reactivity relationships for active site environments in zeolite catalysis. In an effort to provide a perspective that is accessible to readers with varying levels of familiarity with the subject matter, we incorporate brief descriptions of some background concepts about zeolites (with references to external resources containing more detailed discussions) that are helpful to understand the insights presented in this Feature Article. We conclude in Section 4 by providing our outlook on knowledge gaps and future directions that can advance the design of zeolites with tailored active sites for targeted catalytic applications. Throughout this perspective, we underscore our viewpoint that the close integration of precise (post-)synthetic control strategies, validated characterization techniques, well-defined kinetic probes, and properly calibrated theoretical models is important in developing fundamental synthesis–structure–reactivity relationships that underpin the catalytic diversity of active site environments in Brønsted acid zeolites.

2. Active sites within distinct internal void environments of a fixed zeolite framework

The siting of Al at crystallographically distinct lattice positions within zeolite micropores dictates the location of their attendant protons within confining voids of varying sizes and shapes and, in turn, influences the stability of kinetically relevant intermediates and transition states. The structural diversity of zeolites requires brief descriptions of some common metrics used to distinguish relevant void features. The connection of $TO_{4/2}$ building units (T = Si or Al) forms rings (denoted by *X*-MR, where *X* is the number of T-atoms members) and void features such as cavities and channels, which are used to classify zeolite frameworks by the number of T-atoms delimiting their pore apertures into small (8-MR), medium (10-MR), and large (12-MR) pore zeolites.[88,89] The pore limiting diameter (PLD) and the largest cavity diameter (LCD) describe the diameter of the largest sphere that can diffuse through the microporous structure and that can be circumscribed inside zeolitic cavities, respectively.[90–92] In many cases, void shapes can be described by the maximum and minimum diameters of the cross-section (*e.g.*, 0.51 nm × 0.55 nm for MFI sinusoidal channels),[89] while pore dimensionality can be used to describe the ability of guest molecules to diffuse along up to three independent directions (1D; 2D; 3D).[88,89] Further discussions of relevant void and topological features of zeolites can be found elsewhere.[88–98] In this Feature Article, most of our discussions focus on the FER, MFI and MOR zeolite frameworks (Fig. 2).

In this section, we discuss the intermolecular interactions between the organic structure directing agent (SDA) and zeolite framework that underlie synthetic protocols to selectively place Al in desired void environments and the complementary post-synthetic strategies to selectively remove H^+ from undesired void environments. We further describe experimental characterization

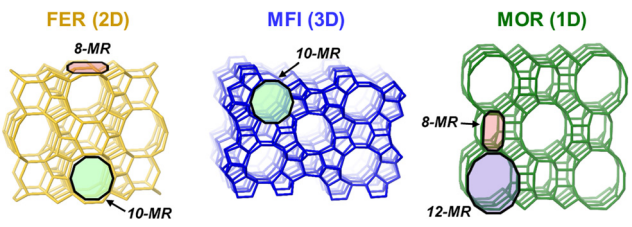

Fig. 2 Void and topological features of three key zeolites (FER, MFI, MOR) discussed in this work. The pore dimensionality and some ring features (8-MR, 10-MR, 12-MR) are indicated. Structures obtained from IZA database.[89]

This journal is © The Royal Society of Chemistry 2024

Open Access Article. Published on 20 September 2024. Downloaded on 1/24/2026 9:35:52 AM.
This article is licensed under a Creative Commons Attribution-NonCommercial 3.0 Unported Licence.

techniques to probe active site locations within distinct zeolite voids. We incorporate discussions of computational assessments that are valuable in developing molecular-level insights into the (post-)synthetic strategies and characterization techniques. We then conclude by using two probe reactions to demonstrate how the catalytic consequences of distinct Al (and H^+) environments of a fixed zeolite framework are elucidated using mechanistic interpretations of rates measured under conditions of strict kinetic control and interpreted alongside theoretical calculations.

2.1. Strategies to control active site placement within distinct void sizes of a fixed framework

2.1.1. Influence of organic SDA on Al siting during synthesis: intermolecular interactions that govern the selective placement of framework Al in distinct zeolite voids. During the hydrothermal synthesis of zeolites, organic molecules, typically quaternary alkylammonium or non-quaternary alkylamine molecules, are used as SDAs in the presence of Al and Si reagents and with the occasional incorporation of alkali cations (*e.g.*, Na^+, K^+) as inorganic co-SDAs. The current understanding of zeolite crystallization processes encompasses a cascade of nucleation and crystal growth stages, in which the local order of organic SDAs and inorganic amorphous aluminosilicate species evolve to form longer range order in periodic crystal lattices.[99–107] Organic SDAs stabilize the formation of a zeolite framework *via* van der Waals (or dispersive) interactions with the silicate species that occlude them and *via* Coulombic (or electrostatic) interactions with the anionic lattice components such as framework Al centers (≡Al–O^-–Si≡) or siloxy defects (≡Si–O^-) (Fig. 3).[99–102,108–112] Beyond stabilizing the incorporation of Al centers into the $SiO_{4/2}$ framework, organic SDAs are also known to influence the siting of Al centers in distinct lattice positions in a manner that is non-random, but with an incompletely understood dependence on synthesis conditions such as the identity and quantity of SDAs.[46,79,80]

Early experimental and theoretical studies recognized how Coulombic interactions influence Al siting at T-sites closest to the charged N^+ center of the organic SDA during synthesis. Using advanced NMR techniques, Shantz *et al.*[113,114] established that during the synthesis of MTW (a 1D large pore zeolite), the cationic N^+ center of the benzyltrimethylammonium organic SDA is preferentially ordered near the anionic framework Al center of the zeolite lattice, consistent with Coulombic type interactions. From these results, they suggested that knowledge of the geometric arrangement of organic SDAs in the zeolite micropores and proper selection of organic SDAs with different charge distributions should be a useful starting point to tune the siting of trivalent framework heteroatoms (*e.g.*, Al) during zeolite synthesis.[113,114] Sastre *et al.*[115,116] used molecular mechanics simulations on ISV (a 3D large pore zeolite with five distinct T-sites) and MEI (a 3D large pore zeolite with four distinct T-sites) to show that Coulombic interactions are maximized (or electrostatic energy minimized) when anionic Al are sited at lattice positions closest to the N^+ center of the organic SDA and that these Coulombic interactions have a greater influence on Al siting than the intrinsic stabilities of Al substitution at distinct T-sites in absence of organic SDA.

Later studies by Pinar *et al.*[117] and Román-Leshkov *et al.*[118] have provided a well-known example of how organic SDAs can bias the relative proportion of H^+ within the smaller 8-MR voids ($H_{8\text{-MR}}^+$; 0.48 nm × 0.35 nm)[89] and the larger 10-MR voids ($H^+_{10\text{-MR}}$; 0.54 nm × 0.42 nm)[89] of FER, a 2D medium-pore zeolite with four distinct T-sites (Fig. 4A). As summarized in Fig. 4B, the synthesis of FER (Si/Al = 10–17) with varying organic SDAs (and combinations thereof), resulted in significant differences in the fraction of H^+ in the 10-MR ($H^+_{10\text{-MR}}/H^+_{\text{total}}$ = 0.11–0.73).[117,118] From Rietveld refinement of powder X-ray diffraction (XRD) data accompanied by molecular mechanics simulations, tetramethylammonium (TMA^+) was found to reside exclusively in the FER cage (accessibly only by 8-MR channel) (Fig. 4), whereas pyrrolidine (Pyrr) or its protonated form (pyrrolidinium; $Pyrr^+$) can reside within either the 10-MR channels or FER cage.[119,120] Molecular mechanics simulations reveal that, in addition to electrostatic interactions with the $[AlO_{4/2}]^-$, $Pyrr^+$ can engage in hydrogen bonding interactions with the anionic oxygen of the $[AlO_{4/2}]^-$ (Fig. 4), which results in a stronger influence of $Pyrr^+$ over TMA^+ on the Al siting in the lattice, especially when Pyrr is occupying the FER cavity.[121] These result in synthesis with Pyrr as the sole organic SDA having the lowest fraction of $H^+_{10\text{-MR}}$ ($H^+_{10\text{-MR}}/H^+_{\text{total}}$ = 0.11), while the addition of TMA^+ to the synthesis media displaces some Pyrr from the FER cavity to the 10-MR channel and results

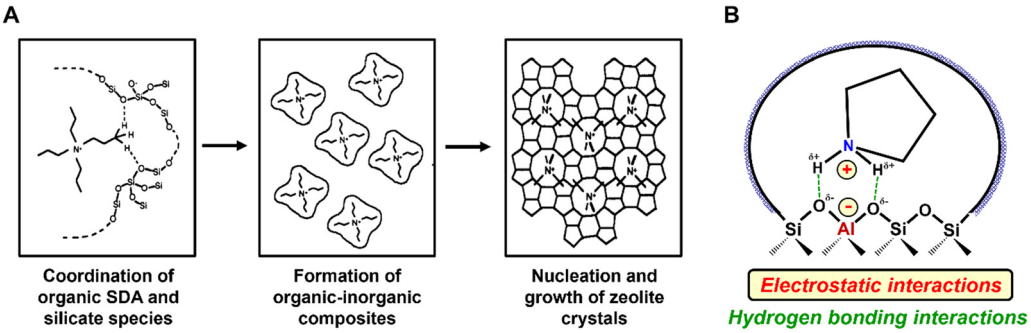

Fig. 3 Roles of organic SDA during zeolite synthesis: (A) stabilizing the crystallization from amorphous precursors *via* van der Waals interactions with silicate species. Adapted from Burkett *et al.*[101,102] (B) Stabilizing the siting of Al at lattice positions *via* electrostatic interactions only (for quaternary organic SDA) and, in some cases, *via* additional hydrogen bonding interactions (in the case of non-quaternary organic SDA).

Open Access Article. Published on 20 September 2024. Downloaded on 1/24/2026 9:35:52 AM.
This article is licensed under a Creative Commons Attribution-NonCommercial 3.0 Unported Licence.

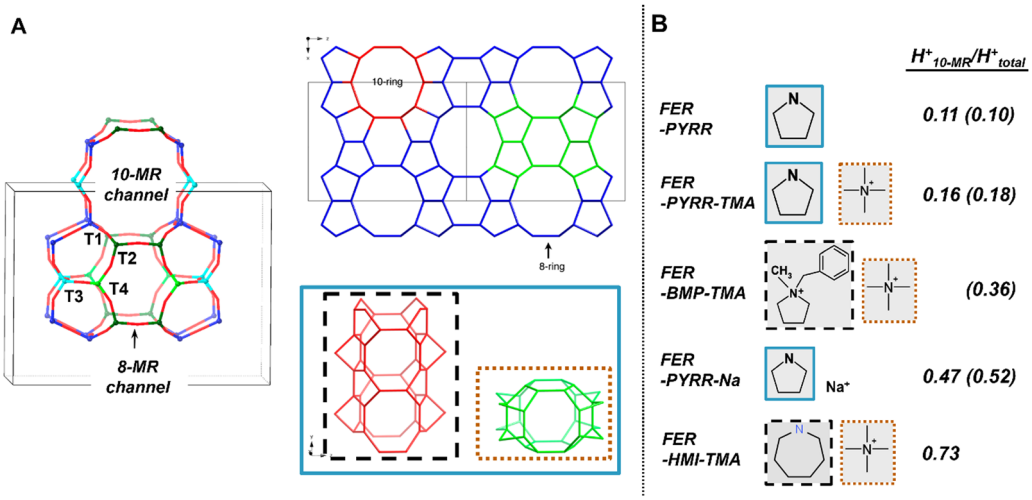

Fig. 4 (A) FER pore structure showing the four distinct T sites, the 10-MR channels, and the ferrierite cavity accessible from 8-MR pore openings. T4 is accessible only from the 8-MR channel. Adapted with permission from Pinar *et al.*[126] Copyright 2021 American Chemical Society and from Pinar *et al.*[119] Copyright 2013 American Chemical Society. (B) Organic SDA used to synthesize FER zeolites and their influence on the H^+ void environment in synthesized FER zeolites. Data for $H^+_{10\text{-MR}}/H^+_{total}$ obtained from Pinar *et al.*[117,119] (shown in parentheses) and Román-Leshkov *et al.*[118] The organic SDAs are color coded by the FER voids that they reside in (A).

in slightly higher fractions of $H^+_{10\text{-MR}}$ ($H^+_{10\text{-MR}}/H^+_{total}$ = 0.16).[117,119] Bulkier organic co-SDAs (>0.50 nm diameter) such as 1-benzyl-1-methylpyrrolidinium (BMP^+)[122,123] or hexamethyleneimine (HMI)[118] are restricted to 10-MR channels because of size exclusion from the smaller FER cage, and this results in increased fractions of $H^+_{10\text{-MR}}$. Furthermore, synthesis using HMI results in the highest fraction of $H^+_{10\text{-MR}}$ ($H^+_{10\text{-MR}}/H^+_{total}$ = 0.73) because hydrogen bonding interactions of the NH_2^+ group and less shielding by the R_2 group (R = alkyl) permit stronger interaction with $[AlO_{4/2}]^-$ in 10-MR relative to the bulkier quaternary alkylammonium structure of BMP^+.[117,118] More recent studies by other groups[124,125] have provided further examples of organic SDAs (morpholine, piperidine, ethylenediamine, pyridine, cyclohexylamine, and 1,6-diaminohexane) that lead to different biases in Al siting in synthesized FER zeolites. Thus, for FER zeolite containing four distinct T-sites with bridging framework O (O_f) atoms that can be oriented in either 8-MR or 10-MR voids, the size and charge distribution (*e.g.*, R_4N^+ *vs.* $R_2NH_2^+$) of the organic SDA dictates the magnitude of its intermolecular interaction with framework anionic Al centers, which determines the siting of Al (and H^+) within distinct void environments (Fig. 4).

In contrast to FER, which contains four crystallographic distinct T-sites in a 2D topology of intersecting and co-planar 8-MR and 10-MR channels, MFI is a lower symmetry framework containing 12 crystallographically distinct T-sites (orthorhombic phase) in a 3D topology of intersecting 10-MR straight (0.53 nm × 0.56 nm) and 10-MR sinusoidal (0.51 nm × 0.55 nm) channels (Fig. 5A) which lie in orthogonal planes that allow for molecular diffusion along the three crystallographic directions.[89,127,128] More importantly, the 12 distinct T-sites of MFI result in 26 distinct neutral O_f atoms for the silicate form (*i.e.*, $\equiv T_a\text{–O–}T_b \equiv$, where $T_a = T_b$ = Si) or 48 distinct anionic O_f atoms for aluminosilicate form (*i.e.*, $\equiv T_a\text{–O}^-\text{–}T_b \equiv$, where $T_a \neq T_b$ = Si or Al) and these bridging anionic O_f can have attendant protons that reside within the channels (~0.55 nm diameter)[92]

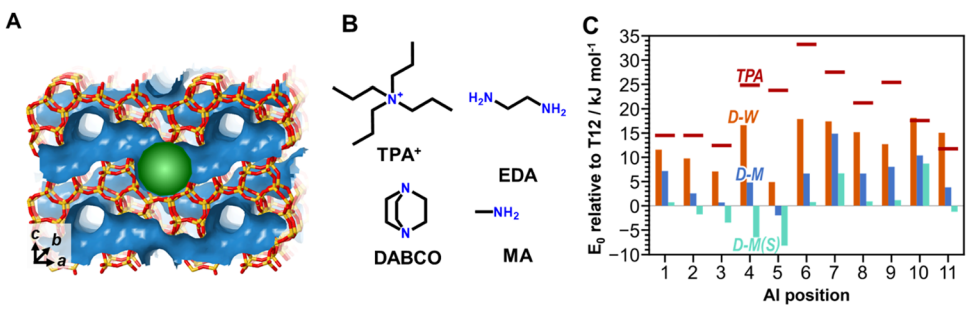

Fig. 5 (A) MFI pore structure showing the sinusoidal channels (blue; across *a*–*c* plane), straight channels (blue; along *b*-axis), and the channel intersections (green) (B) Conventional organic SDA (TPA^+) and nonconventional organic SDA mixtures (EDA + TPA, DABCO + MA) used to synthesize MFI zeolites. (C) Energies of Al siting in positions T1–T11 (relative to T12) with varying organic SDA complexes: D-W = $[DABCO\text{-}H\text{-}H_2O]^+$, D-M = $[DABCO\text{-}H\text{-}MA]^+$; (S) indicates calculation performed with an implicit solvation model. Reproduced with permission from Ezenwa *et al.*[131] Copyright 2024 American Chemical Society.

 This journal is © The Royal Society of Chemistry 2024

Open Access Article. Published on 20 September 2024. Downloaded on 1/24/2026 9:35:52 AM. This article is licensed under a Creative Commons Attribution-NonCommercial 3.0 Unported Licence.

or their larger intersections (~0.70 nm diameter).[92,129,130] The increased structural complexity of MFI zeolite framework (relative to FER) present various synthetic challenges to precisely tune the void location of the proton. To illustrate, each isolated Al-substituted T-site of MFI has four possible bridging O_f–H that are isoenergetic (*i.e.*, DPE within 10 kJ mol^{-1})[7] and can host protons in either channel or intersection void environments, with the exception of T4 site that can only host protons accessible in the sinusoidal channel environments.[130]

The synthesis of MFI zeolites using the conventional tetra-*n*-propylammonium (TPA^+)[132] SDA (Fig. 5B) is known to preferentially position $[AlO_{4/2}]^-$ in T-sites bordering the larger intersections and that are closest to the N^+ center of the TPA^+ molecules that are fixed at MFI intersections, because electrostatic interactions are maximized when the N^+–Al^- distance is minimized.[130,133,134] Yokoi and colleagues[135–138] reported that the synthesis of MFI zeolites (Si/Al = 20–50) using mixtures of alkylamine (*e.g.*, cyclohexylamine) or alcohol (*e.g.*, pentaerythritol, PET; trimethylolethane, TME) molecules and Na^+ resulted in increased siting of Al at T-sites within the more constrained channel environments because neutral branched organic molecules occupy intersection voids, thereby forcing Na^+ to charge compensate Al centers (Na^+/Al = 0.3–1.1)[135,137] at channel environments. We note that prior to these reports,[135–137] MFI zeolites had been synthesized with >30 different types of organic molecules[132,139–157] but with scant reports[79] of the resulting consequences on Al siting within different voids during synthesis with non-conventional organic SDA. Further studies by other research groups[158–162] also reported or inferred that MFI synthesized using the earlier reported alcohol molecules (PET, TME)[136,137] or *n*-butylamine (NBA)[158,160] resulted in increased siting of Al at the channel environments relative to the intersection environments that are favored by TPA^+. A recent study by Yokoi and colleagues[163] further proposed that PET molecules prevented the interaction of TPA^+ molecules and $[AlO_{4/2}]^-$ centers thereby enhancing the ability of Na^+ to place Al centers in channels during synthesis of MFI using mixtures of TPA^+, PET and Na^+. However, detailed molecular-level insights into the influence of organic SDA structure on Al siting remain limited for MFI zeolites.

Recently, we reported[131] that the synthesis of MFI zeolites of fixed Al content (Si/Al ≈ 50) using an either an equimolar mixture of 1,4-diazabicyclo[2.2.2]octane (DABCO) and methylamine (MA)[164] or a mixture of excess ethylenediamine (EDA) with minor quantities of TPA^+,[165] resulted in significant bias of Al towards the more confined channels. In contrast, the synthesis of MFI zeolites using TPA^+ as the only SDA resulted in the predominant siting of Al within the larger intersections, in agreement with density functional theory (DFT) studies.[130,133] In the case of MFI crystallization using DABCO/MA mixtures, DFT simulations reveal that the ability of protonated DABCO complexes to reorient within MFI intersections and participate in additional hydrogen-bonding interactions with $[AlO_{4/2}]^-$ stabilizes a broader range of Al substitution locations and facilitates the placement of Al at T sites in the smaller channel environments that are less favored by TPA^+ (Fig. 5C).[131] We surmised that a similar flexibility and ability of protonated EDA to form H-bonding interactions biases the Al positioning away from the intersection-dominant locations preferred solely by TPA^+.[131] Indeed, earlier studies by Perego and colleagues[148,149] reported that EDA molecules are stabilized by favorable van der Waals interactions in the smaller channels of MFI and that the compositional N/B ratio ~1 in samples crystallized from borosilicate solutions implies that EDA interacts with framework B either *via* electrostatic interactions in their protonated form or *via* N···H–O_f hydrogen bonds in their unprotonated form,[148,149] suggesting a similar mechanism by which EDA may bias the siting of trivalent heteroatoms towards channels. Furthermore, the findings from our group[130,131] are consistent with those of a recent DFT and molecular dynamics (MD) study that proposed that organic SDAs with different charge distributions and mobility within voids can alter the Al siting towards T-sites that are further away from MFI intersections.[133] Together, these molecular-level details depict a mechanistic link between organic SDA structure and Al siting in MFI zeolites.

Seldom examined in prevailing discourses on organic SDA influence during zeolite synthesis, H-bonding interactions have been proposed to play a significant role in the assembly of organic guest molecules within diverse inorganic microporous hosts (*e.g.*, aluminosilicates, aluminophosphates, zincophosphates, gallogermanates)[121,166–171] For instance, H-bonding interactions between tris(ethylenediamine)cobalt(III) complexes ($[Co(en)_3]^{3+}$) and aluminophosphate frameworks were reported to promote the crystallization of aluminophosphates and transfer the chirality of the metal complex to the inorganic hosts.[166,167,170] Furthermore, Gómez-Hortigüela and colleagues used molecular simulations to identify that strong H-bonding interactions between flexible organic molecules containing H-bond forming groups (–NH or –OH) and the O_f atoms bridging isomorphically substituted lower-valent dopants (*e.g.*, Mg^{2+} for Al^{3+} in AFI aluminophosphates[168,169] or Al^{3+} for Si^{4+} in FER aluminosilicates[119,121]) drive the siting of dopants in the framework.[172] These insights demonstrate that a computationally informed choice of organic molecule capable of participating in hydrogen bonding interactions with the zeolite framework may be an important design strategy to place active sites in desired environments.[131]

Further notable examples of the influence of organic SDAs on framework Al siting for a fixed zeolite framework can be found in reports for (a) MOR, a 1D large-pore zeolite containing four distinct T-sites distributed among 8-MR side-pockets (0.57 nm × 0.26 nm; 0.48 nm × 0.34 nm) and 12-MR channels (0.70 nm × 0.65 nm),[173–177] (b) RTH, a 2D small-pore zeolite with four distinct T-sites distributed among non-distorted 8-MR (0.41 nm × 0.38 nm) and distorted 8-MR (0.56 nm × 0.25 nm) pore apertures,[178] (c) MWW, a 2D medium-pore zeolite containing eight distinct T-sites (up to 14 T-sites for SSZ-70) distributed among 10-MR sinusoidal channels within layers (0.51 nm × 0.41 nm) and 12-MR supercages (0.71 nm × 0.71 nm) with 10-MR apertures between layers (0.55 nm × 0.40 nm),[179,180] and (d) IFR, a 1D large-pore zeolite containing

Open Access Article. Published on 20 September 2024. Downloaded on 1/24/2026 9:35:52 AM. This article is licensed under a Creative Commons Attribution-NonCommercial 3.0 Unported Licence.

four distinct T-sites within the 12-MR channel (0.62 nm × 0.72 nm).[181]

Together, experimental and computational studies demonstrate that beyond intrinsic (*i.e.*, thermodynamically preferred under SDA-free conditions) Al siting preferences at crystallographic distinct T-sites and van der Waals interactions that stabilize organic SDAs within specific pore geometries, intermolecular interactions (*e.g.*, electrostatics, hydrogen bonding) between organic SDAs and Al centers play a major role in the placement of framework Al at distinct T-sites; such interactions depend on the size, structure, chemical functionality, and charge distribution of organic SDAs and their mobility within the voids during crystallization.

2.1.2. Selective removal of acid sites in distinct voids *via* post-synthetic modification. Following zeolite crystallization, the Al siting in the resulting inorganic solid is thought to be more deterministic and less stochastic in nature.[46,79,80] However, predictive design rules for Al siting in zeolites are yet to be fully realized because of the complex nature of hydrothermal crystallization involving kinetically and thermodynamically controlled cascades of nucleation, growth, and dissolution processes to form a metastable framework[103] and the complex structure of many zeolites that can contain >4 symmetry distinct T-sites and an even higher number of distinct bridging O_f that charge compensate the H^+ sites.[46] Post-synthetic design approaches (Fig. 6) can provide an alternative and complementary route to tune H^+ location by selectively removing H^+ and framework Al in undesired void environments and lattice positions, respectively.

The post-synthetic treatment of MOR zeolites in aqueous Na^+ solutions at sub-unity Na^+ to Al molar ratios is a well-known technique to preferentially exchange H^+ in the 8-MR side pockets ($H_{8\text{-MR}}^+$) with catalytically inactive Na^+ while preserving H^+ in 12-MR channels ($H_{12\text{-MR}}^+$),[11,182–185] because of closer contacts of Na^+ cations with framework oxygen atoms within smaller 8-MR voids than those within larger 12-MR voids.[11] On the other hand, $H_{12\text{-MR}}^+$ are preferentially poisoned by pyridine or alkylpyridines (*e.g.*, 2,6-dimethylpyridine),[174,185–187] exchanged by tetramethylammonium ions,[188] or eliminated *via* silylation with trimethylchlorosilane[189] because size constraints exclude these bulky species from accessing $H_{8\text{-MR}}^+$. Furthermore, as surmised by a recent experimental and theoretical study[13] from our group that found that Na^+ preferentially titrated H^+ in 6-MR Al–Al pair configurations over H^+ at isolated Al sites in CHA zeolites, strong effects of preferential Na^+ titration of H^+ within distinct void environments of aluminosilicates may reflect an underlying influence of Al–Al pairs. Thus, the selective titration of H^+ sites is a post-synthetic approach to tune the H^+ void environments in certain zeolites.

The selective deposition of unreactive organic residues in specific voids provides another established strategy to post-synthetically tune H^+ siting in zeolites with independent non-connected pore systems. During the cracking of *n*-hexane and 3-methylpentane (588 K) in MOR, $H_{12\text{-MR}}^+$ were preferentially deactivated with time-on-stream when compared to $H_{8\text{-MR}}^+$.[190] Similarly, H^+ located within 12-MR supercages of MWW zeolites (0.71 nm × 0.71 nm) were preferentially deactivated with time-on-stream over H^+ located within the 10-MR sinusoidal channels (0.51 nm × 0.41 nm) during *n*-hexane and 3-methylpentane cracking (588 K),[190,191] *n*-heptane cracking (623–723 K),[192–194] *m*-xylene transformation (623 K),[195,196] toluene methylation (623 K),[30,31] methanol to hydrocarbons (723 K),[197,198] and syngas to gasoline (633 K).[199] However, for certain zeolite topologies with interconnected pore systems (*e.g.*, MFI), deposition of bulky organic residues imprecisely alters the Al siting and may introduce unintended collateral effects, given that blocking of H^+ sites in intersections will restrict access to H^+ sites in the connected channels and *vice*

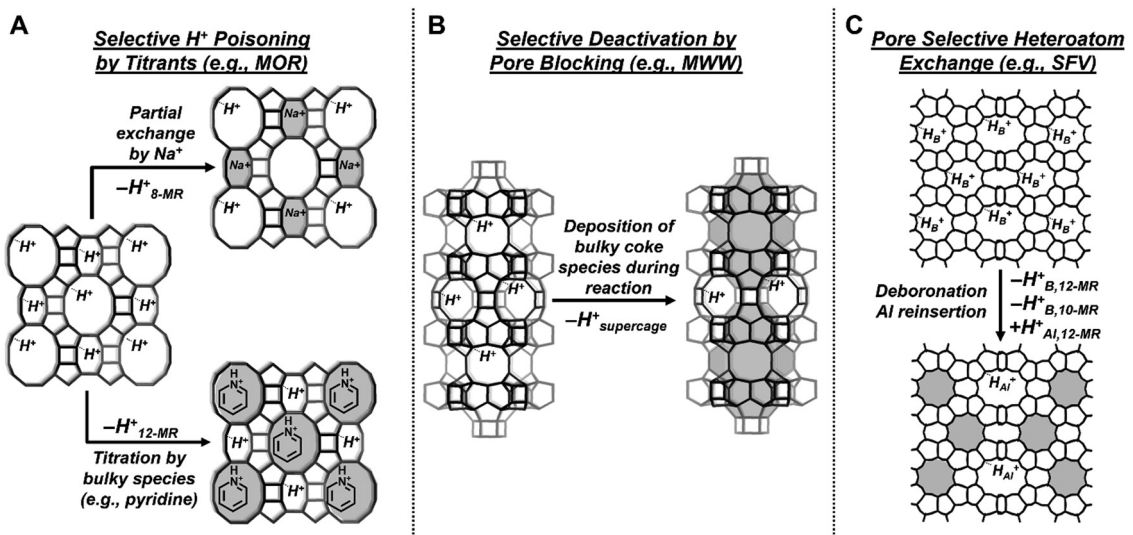

Fig. 6 Schematic summarizing the highlighted post-synthetic techniques to modify Al and H^+ siting within distinct micropore environments of zeolites. (A) Selective poisoning of H^+ sites in 8-MR and 12-MR of MOR by Na^+ or bulky titrants, respectively. (B) Selective deactivation by pore blocking of H^+ sites in 12-MR supercages of MWW zeolites. (C) Selective heteroatom exchange in SFV zeolites. Shaded regions depict voids containing inactive sites.

 This journal is © The Royal Society of Chemistry 2024

Open Access Article. Published on 20 September 2024. Downloaded on 1/24/2026 9:35:52 AM. This article is licensed under a Creative Commons Attribution-NonCommercial 3.0 Unported Licence.

versa. Nevertheless, the selective deposition of coke species remains a viable technique to post-synthetically eliminate H^+ sites within distinct void environments of certain zeolites containing non-intersecting pore systems.

Selective exchange of trivalent heteroatoms of different reactivities in distinct voids of zeolites is an emerging design strategy to post-synthetically introduce Al to specific void environments of zeolites. For example, H^+ that charge-compensate framework boron (H_B^+) are typically catalytically irrelevant relative to H_{Al}^+ because the DPE of H_B^+ is ~70 kJ mol^{-1} higher than that of H_{Al}^+.[200–203] The synthesis of borosilicate zeotypes followed by deboronation and subsequent Al reinsertion (B → Al exchange) has historically provided an indirect route to obtain certain aluminosilicate zeolites that are inaccessible from direct crystallization using amorphous Al reagents.[204–206] Beyond synthesizing new zeolite frameworks, Zones, Koller and colleagues further observed that (i) in certain zeolites, B atoms typically site at structural motifs such as 4-ring chains,[207,208] (ii) hydrated Al^{3+} cations are unable to access 10-MR pores,[207,209] (iii) heteroatom siting is preserved during B/Al exchange without significant T-site or silanol nest migration.[207,208] These observations suggest that B → Al exchange might be a viable strategy to tune Al siting in certain zeolite frameworks, a process referred to as "pore selective aluminum reinsertion".[206] This was demonstrated for post-synthetically B → Al exchanged SFV (SSZ-57) zeolites that contained Al in only 12-MR pores[209] as opposed to directly synthesized Al-SFV zeolites that contained Al in both 12-MR and 10-MR pores.[210,211] Such emerging techniques to selectively reinsert Al into specific lattice positions hold promise, but find limited applications for medium-pore zeolites as reported earlier[207,209] and observed in our own unpublished studies. Alternative strategies such as gas-phase Al exchange in moisture-free atmospheres or liquid-phase exchange in moisture-free solvents[212] into deboronated zeolites could be explored to overcome the current hurdles for medium-pore zeolites and allow the indirect synthesis of aluminosilicates with tailored Al siting than would have been obtained if synthesized directly in Al-containing form.

2.2. Experimental characterization of Al siting within distinct voids

Synthetic and post-synthetic strategies to tune the siting of Al (and attendant H^+) within distinct voids of zeolites require characterization techniques to assess the resulting impact on Al siting within distinct voids. These techniques are broadly distinguished by those that seek to identify the lattice position of framework Al and those that seek to determine the void environment of the protons directly without adsorbed probes or indirectly using adsorbed probes.

Solid-state ^{27}Al magic angle spinning nuclear magnetic resonance (MAS NMR) spectra are sensitive to differences the local coordination environments of ^{27}Al nuclei and are widely used to distinguish tetrahedrally coordinated framework Al (~54–65 ppm) from octahedrally coordinated extra-framework Al species (~0 ppm).[213] The early reported correlation by Lippmaa *et al.*[214] of ^{27}Al chemical shifts with the average Al–O–Si bond angles in various Al-rich aluminosilicates (Si/Al = 1–5) suggests that ^{27}Al MAS NMR may be able to capture subtle differences in the local structure of framework Al due to differences in Al siting among distinct lattice positions. Han *et al.*[215] reported that two observed peaks (~51.2 and ~53.5 ppm) in both the ^{27}Al MAS NMR and the two-dimensional ^{27}Al triple-quantum (3Q) MAS NMR spectra of MFI zeolites (Si/Al = 14–250) result from overlapped signals of two subsets of the 12 distinct T-sites, and further used the correlation by Lippmaa *et al.*[214] and Al–O–Si angles from the crystallographic data of Olson *et al.*[128] to estimate isotropic ^{27}Al chemical shifts for the 12 distinct T-sites of orthorhombic MFI.

Subsequent studies by Sklenak *et al.*[216–218] combined ^{27}Al 3Q MAS NMR experiments and quantum mechanics molecular mechanics (QM/MM) simulations to perform a partial assignment of observed resonances to specific T-sites in monoclinic MFI (24 distinct T-sites). They noted that no simple correlation exists between ^{27}Al isotropic chemical shifts and average calculated Al–O–Si angles and that the crystallographic X-ray data contained artefacts in Al–O–Si bond angles because of low Al content. Nevertheless, studies by Han *et al.*,[215] Sklenak *et al.*,[216–218] and by other groups (including ours)[130,131,134,137,219,220] agree on the non-random siting of Al at distinct T-sites of MFI zeolites synthesized using TPA^+. However, across these studies on MFI and on other low symmetry zeolites containing >4 distinct T-sites,[179,221–225] the majority (>90%) of the isotropic ^{27}Al chemical shifts fall within a narrow range (<10 ppm)[219] and result in experimental ^{27}Al signals that are still too close to be unambiguously resolved despite advances in multiquantum (MQ) MAS experiments and increases in NMR resolution in recent years.[226,227] On the other hand, for zeolite topologies (FER,[125,228,229] RTH,[178] IFR[181]) of higher symmetry containing 4 distinct T-sites, the ^{27}Al 1D or 2D MQ MAS NMR spectra can be partially resolved into at least two components that significantly change with varying synthesis organic SDA at fixed solid Si/Al ratios (Fig. 7).

Besides NMR techniques, X-ray diffraction (XRD) methods have been applied to deduce the lattice positions of framework heteroatoms (*e.g.*, Al, B) through locating the positions of well-ordered organic SDA molecules in as synthesized zeolites.[230] In this approach, the single-crystal or powder XRD data are processed using Rietveld refinement[231] to obtain positional parameters for the atoms of the inorganic zeolite host and the organic SDA guest. The refined interatomic distances between the C and N of the organic SDA and the O_f atom are used alongside interaction energies calculated using molecular simulations (MM or MD) to draw conclusions on the highest probability locations of the organic SDA and the anionic Al centers bearing O_f that are closest to the N^+ center of the organic SDA. This approach has been partly successful in determining the preferred lattice positions of framework Al in FER zeolite synthesized using varying organic SDA (described in Section 2.1.1)[119,120,124] and of framework B in various zeolite frameworks.[230,232,233] In addition to challenges in distinguishing framework Si from Al because of their similar scattering

Open Access Article. Published on 20 September 2024. Downloaded on 1/24/2026 9:35:52 AM.
This article is licensed under a Creative Commons Attribution-NonCommercial 3.0 Unported Licence.

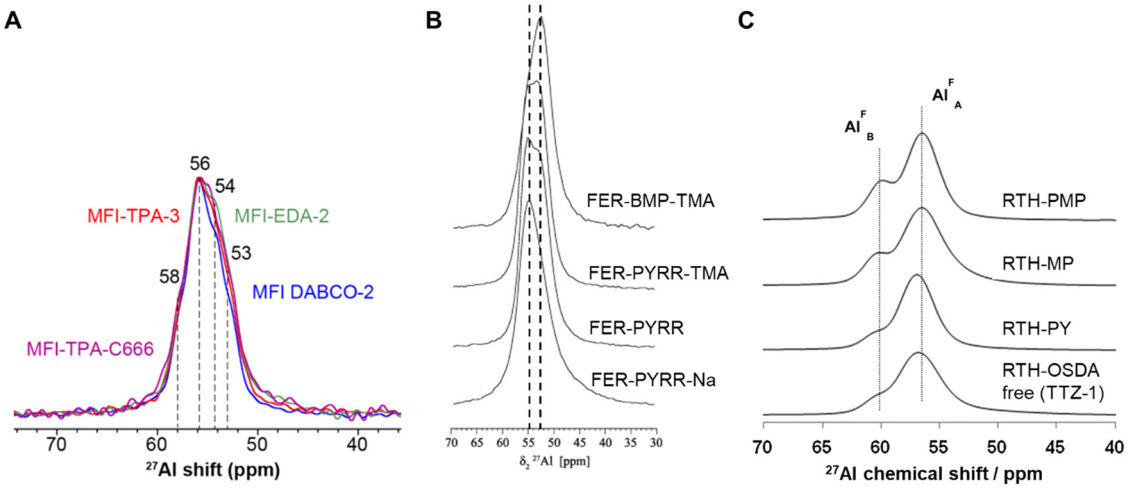

Fig. 7 Solid-state 1D ^{27}Al MAS NMR spectra of (a) MFI, (b) FER, (c) RTH zeolites synthesized using varying organic SDA. Adapted with permission from Ezenwa *et al.*,[131] Pinar *et al.*,[228] and Liu *et al.*,[178] respectively. Copyright 2024 American Chemical Society, 2014 Elsevier, 2014 Royal Society of Chemistry The spectra show qualitative differences which suggest that the various OSDA biased locations of framework Al among various lattice positions.

factors,[119,120] structural refinements of powder XRD patterns are also limited by lower contrast of organic guests because of their lighter scattering relative to the inorganic host, low symmetry of occluded organic SDA, and low resolution of intensities from overlapping diffraction planes.[230]

Techniques such as simulated annealing,[234] a systematic global optimization routine, have been used to improve the extraction of locations of organic SDA and framework heteroatoms from structural refinement of powder XRD patterns.[230,232] In addition, XRD data collected at the Al K-edge, where the Al scattering factor significantly diverges from that of Si because of resonant scattering (termed anomalous X-ray diffraction), has been combined with conventional powder XRD data to unambiguously and quantitatively determine the occupancies of Al at the four distinct T-sites of two H-form FER zeolites synthesized using different organic SDAs (Fig. 8).[126] Thus, powder XRD data when obtained at the Al K-edge[126] or when refined using simulated annealing[230] could enable locating the position of framework Al in lower symmetry zeolite frameworks (*e.g.*, MFI). Additional X-ray based techniques such as extended X-ray absorption fine structure (XAS) spectroscopy,[223,224] Al valence-to-core X-ray emission spectroscopy (XES)[235] and fluorescence spectroscopy using X-ray standing waves (XSW)[236] have also been used to estimate the occupation of distinct T-sites by Al in BEA (9 T-sites), FER (4 T-sites) and NAT (2 T-sites) zeolite, respectively.

In contrast to techniques used to identify the lattice positions of framework Al, alternative approaches measure differences in H^+ environments, which are then mapped to the most probable framework Al positions, given knowledge of void environments of their bridging O_f atoms and assumptions of isoenergetic distributions of associated H^+. During infrared (IR) spectroscopy of H-form zeolites, the O_f–H^+ bond stretching frequencies (ν_{OH}) for Brønsted acid sites are known to be sensitive to void environments as reflected in a wide range of ν_{OH} (3550–3660 cm^{-1}) across zeolites of varied framework topologies that contain differently sized void environments.[7,237–246] In addition, reported molar extinction coefficients for Brønsted acid sites (ε_{OH}) are either similar or vary (2–20 cm μmol^{-1}) with void size.[183,238,245–248] These variations have been broadly ascribed to O_f–H^+ bonds perturbed *via* interactions with nearby O_f atoms regardless of the specific

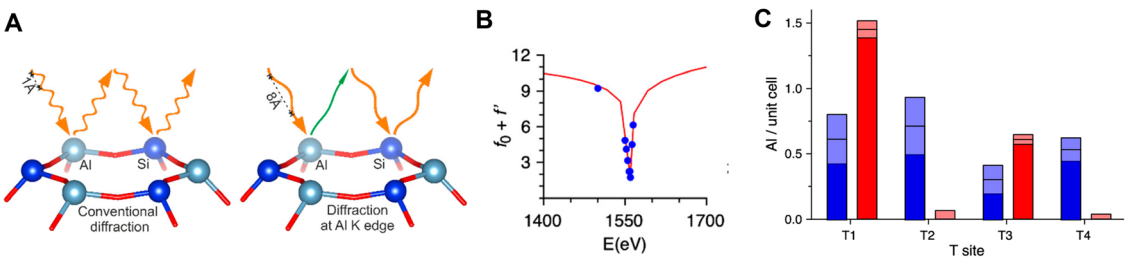

Fig. 8 (A) Illustration of anomalous X-ray scattering at the Al K edge (1.56 keV or 7.95 Å) as an approach to distinguish the similar scattering factors of Al and Si within FER zeolites containing Si/Al ratios >5. (B) The real part ($f_0 + f'$) of the X-ray scattering factor ($f = f_0 + f' + if''$) as a function of the X-ray energy. Within the vicinity of the Al K edge, the f' and f'' become more significant than f_0 (the number of electrons) which changes the scattering power of Al. (C) Distribution of Al among four distinct T-sites in two FER zeolites (2.2 Al per unit cell) of varying synthetic origins. Reproduced with permission from Pinar *et al.*[126] Copyright 2021 American Chemical Society.

 This journal is © The Royal Society of Chemistry 2024

Open Access Article. Published on 20 September 2024. Downloaded on 1/24/2026 9:35:52 AM.
This article is licensed under a Creative Commons Attribution-NonCommercial 3.0 Unported Licence.

nature (electrostatic,[241] hydrogen bonding,[242–244,248–250] or van der Waals[7]), where smaller voids offer more intimate interactions that lengthen O_f–H^+ bonds and decrease ν_{OH}.[7,241–244]

The IR spectra of various H-MOR zeolites with a narrow composition (Si/Al = 6–10), but varied commercial origins, were found to consist of an asymmetric IR band in the Brønsted acid O_f–H^+ stretching region which can be deconvoluted into two symmetric bands arising from $H_{8\text{-MR}}^+$ (~3590 cm^{-1}) and $H_{12\text{-MR}}^+$ (~3610 cm^{-1}) (Fig. 9A).[11,182–186] Among these MOR samples, the ratios of $H_{8\text{-MR}}^+$ and $H_{12\text{-MR}}^+$ to H^+_{total} varied with sample origin[11,182–186] and with selective poisoning of either $H_{8\text{-MR}}^+$ by Na^+ cations[11,182–185] (Fig. 9B) or $H_{12\text{-MR}}^+$ by (alkyl)pyridines;[185,186] these indicate that the unreported synthetic origins resulted in non-random siting of Al among the four symmetry distinct T-sites and, in turn, non-random distribution of H^+ among the 10 distinct O_f atoms. Recent studies on MOR zeolites have further reported that varying organic SDA at fixed Al and total H^+ contents biases the relative proportions of $H_{8\text{-MR}}^+$ and $H_{12\text{-MR}}^+$, measured *via* deconvolution of O_f–H^+ IR spectra.[175,176] However, across various research groups, quantitative assessments of H^+ locations within distinct MOR voids vary with spectral deconvolution procedures that differ in numbers of primary components and in optimization routines for spectral features (*e.g.*, peak shape and positions).[175,176,183,185,251] In addition, values of ε_{OH} and ν_{OH} depend not only on intermolecular interactions with the nearby void environment[7,241–244] but also on the local configurations of proximal H^+ that are sensitive to temperature even for high-symmetry zeolites containing one crystallographic distinct T-site (*e.g.*, FAU,[252] CHA[13,253]).

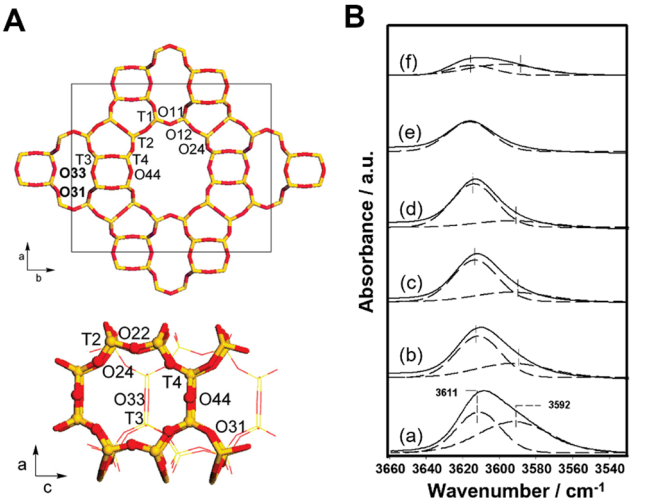

Fig. 9 (A) MOR framework structure showing the four distinct T sites and some framework O sites. T3–O31 and T3–O33 positions are located exclusively in the 8-MR side-pockets. The rest of the T–O_f pairs are either located within the 12-MR channel or at the boundary between the 8-MR side pockets and the 12-MR channels. Adapted with permission from Boronat *et al.*[254] Copyright 2008 American Chemical Society (B) Deconvolution of OH IR spectra of on a series of partial Na^+-exchanged MOR zeolites (Si/Al = 10; (a)–(f) reflects increasing degree of Na exchange (Na/Al = 0.00, 0.17, 0.27, 0.41, 0.55, 0.90)). Reproduced with permission from Bhan *et al.*[185] Copyright 2007 American Chemical Society.

The accessibility of probe molecules to distinct voids of certain zeolites has been used to quantify differences in H^+ environment.[244,255] Specifically, the adsorption of pyridine (kinetic diameter, d_{kin} ~ 0.58 nm) on H-form zeolites followed by quantification using IR or NMR spectroscopy is a common procedure for quantifying H^+ sites in pores with apertures larger than those of 8-MR (~0.40 nm diameter).[238,244,255] This approach has enabled the quantification of $H_{12\text{-MR}}^+$ of MOR zeolites[182,185,186] and $H^+_{10\text{-MR}}$ of FER zeolites[117,118] because pyridine cannot access $H_{8\text{-MR}}^+$. However, reproducible quantification for certain zeolites can be limited by partial accessibility of pyridine to H^+ sites because of slow diffusion rates during the timescale of the experiments and by variations in molar extinction coefficients for the ring vibration bands or the N–H^+ stretching bands of pyridinium ions.[255–257] In addition, for zeolites containing distinct but interconnected pore environments (*e.g.*, ~0.55 nm channels and ~0.70 intersections of MFI), pyridine indiscriminately titrates all H^+ sites, thus preventing the quantification of distinct site environments.

The constraint index (CI) test,[258] given by *n*-hexane-to-3-methylpentane cracking rate ratio (typically between 623–673 K), is one of many catalytic probe reactions[259] that have been historically developed to assess differences in void features (limiting aperture size and void connectivity) of zeolite frameworks. In cases where reactivity is weakly influenced by intracrystalline diffusion limitations, the CI test may also sense the influence of active site environments on the stabilities of differently sized transition states.[258,259] However, CI test values deviate from expected trends for certain zeolite topologies,[190,191] are sensitive to presence of independent pore systems that deactivate at different rates (*e.g.*, MOR and MWW),[190] and vary significantly with temperature[258] for medium-pore zeolites because of competition either between enthalpic and entropic effects[260] or between monomolecular and bimolecular mechanisms.[261,262] Nevertheless, MFI synthesized using certain non-conventional organic molecules (*e.g.*, PET, TME, NBA) were reported to have higher CI test values relative to MFI samples synthesized using TPA^+, which was used to infer that non-conventional MFI samples contained significant numbers of active sites within the more constrained channel environments.[135,137,158–160,163]

Together, the merits and drawbacks of the highlighted characterization techniques for assessing differences in framework Al siting or in H^+ void environments pinpoint areas to advance the development of improved techniques that unambiguously quantify active sites within distinct void environments, even among lower symmetry frameworks such as MFI and MWW zeolites.

2.3. Catalytic consequences of acid site location in distinct void environment of a given zeolite

Under conditions where catalysis is not influenced by constraints on molecular diffusion within micropores, reactivity and selectivity differences across zeolites reflect the effects of pore confinement on the stabilities of intermediates and transition states at active sites within voids environments of varying

Open Access Article. Published on 20 September 2024. Downloaded on 1/24/2026 9:35:52 AM. This article is licensed under a Creative Commons Attribution-NonCommercial 3.0 Unported Licence.

sizes and shapes.[38,39] Confinement effects reflect attractive van der Waals interactions between bound species and confining voids that offset the energy penalties associated with the structural distortions required to accommodate organic guests within inorganic host and the entropic losses of bound species upon confinement.[32,43,44,263–265] Furthermore, confinement effects become more significant when transition states and their precursors or other competing transition states are solvated to different extents because of differences in sizes.[39] Elucidating the catalytic consequences of active site environments requires maintaining the link between reactivity and the local structures of active sites and bound species;[38] this necessitates measurement of rates and selectivity in absence (or accounting for) intracrystalline diffusion constraints while minimizing the contributions of side reactions that often convolute kinetic, thermodynamic and transport phenomena.[44,77,266–268] There are many examples of complex reaction networks that are reported to be sensitive to differences in active site environments in a given zeolite (*e.g.*, methanol to hydrocarbons in MFI, MEL, MWW[137,159,197,269–271]), but for the aforementioned reasons, we do not discuss those in this perspective. Rather, in this section, we use the methylations of carbon monoxide (CO) and toluene by DME at low reaction temperatures (<473 K) to demonstrate how the active site environment alters kinetically controlled reactivity and selectivity for a given zeolite framework with fixed active site density but of varying synthetic origin.

2.3.1. Preferential stabilization of transition states over intermediates during CO methylation in 8-MR voids of MOR and FER zeolites. The methylation of CO by DME, also known as DME carbonylation, produces methyl acetate and occurs with high rates and selectivity at low temperatures (400–500 K) on Brønsted acid zeolites containing 8-MR voids (*e.g.*, MOR and FER).[185,272–274] During CO methylation on MOR zeolites (423–463 K), methyl acetate formation rates are first order in CO pressure P_{CO}; 0–930 kPa (Fig. 10A) and zero-order in DME pressure (0.8–67 kPa), reflecting active sites covered by DME-derived species such as surface methyls (CH_3–Z) or trimethyloxonium species ($CH_3O(CH_3)_2^+Z^-$).[275,276] Steady-state and transient kinetic, isotopic, spectroscopic and titrimetric experiments evidence the involvement of surface methyls that react with gas-phase CO in a kinetically relevant C–C bond formation step to form surface acetyls, which subsequently react with DME in a kinetically irrelevant step to form methyl acetate.[275,276] Methyl acetate formation rates (per g zeolite; 438 K) strictly depend on the number of H^+ sites in 8-MR voids (per g zeolite; quantified *via* IR spectroscopy) on a series of partial Na^+ exchanged MOR and H-FER zeolites (Fig. 10B).[185] A mechanism-derived rate expression (eqn (1)) describes the methyl acetate formation rates (r_{Ac}; per H^+) in terms of the kinetically relevant rate constant (k_{Ac}) and P_{CO}:[276]

$$\frac{r_{Ac}}{[H^+]} = k_{Ac} P_{CO} \quad (1)$$

Using transition state theory,[277,278] k_{Ac} is further described in terms of the Gibbs free energy barrier ($\Delta G_{act,Ac}$) to form the kinetically relevant CO methylation transition state from a surface methyl and a CO molecule in the extracrystalline gas phase (eqn (2); Fig. 11):[39]

$$k_{Ac} = \frac{k_B T}{h} e^{\frac{-\Delta G_{act,Ac}}{RT}} \quad (2)$$

The reactivity of H^+ sites contained within 8-MR voids of MOR

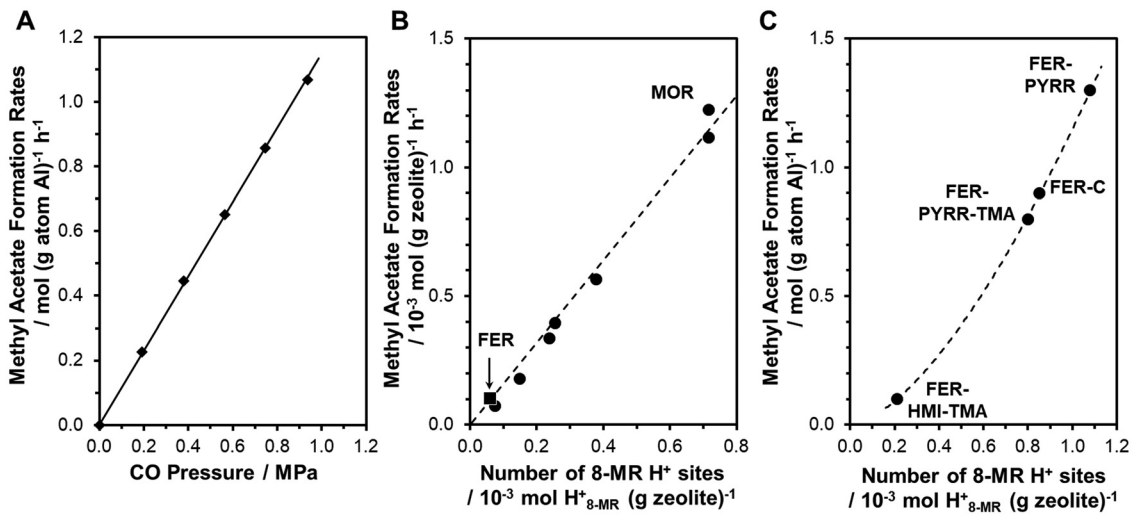

Fig. 10 (A) Methyl acetate formation rates (per g Al) as a function of CO pressure during CO methylation (438 K) by DME (2–16 kPa) on H-MOR zeolite (Si/Al = 10). Solid lines represent regressed best fit to eqn (1). Adapted with permission from Cheung *et al.*[275] Copyright 2006 Wiley-VCH (B) Methyl acetate synthesis rate (per g zeolite; 438 K, 930 kPa CO, 20 kPa DME) as a function of number of H^+ in 8-MR of Na,H-MOR and H-FER zeolites (per g zeolite). Dashed line represent line of best fit for MOR data. Adapted with permission from Bhan *et al.*[185] Copyright 2007 American Chemical Society (C) Dependence of methyl acetate synthesis rate (per g Al; 473 K, 166 kPa CO, 100 kPa DME) on number of H^+ in 8-MR of H-FER zeolites synthesized using varying organic SDA (FER-Pyr, FER-TMA, FER-HMI-TMA; Section 2.1.1) or obtained from a commercial source (FER-C). Adapted with permission from Román-Leshkov *et al.*[118] Copyright 2011 American Chemical Society. Dashed line serves to guide the eye.

 This journal is © The Royal Society of Chemistry 2024

Open Access Article. Published on 20 September 2024. Downloaded on 1/24/2026 9:35:52 AM. This article is licensed under a Creative Commons Attribution-NonCommercial 3.0 Unported Licence.

or FER zeolites reflects the ability of the confining environment (~0.40 nm average diameter) to preferentially stabilize the larger CO methylation transition state over the smaller surface methyl precursor *via* favorable van der Waals contacts, thereby decreasing activation barriers (Fig. 11).[38,39] Dispersion-corrected DFT calculations also reveal that the specificity of $H_{8\text{-MR}}^{+}$, results from the unique orientation of the surface methyl intermediate and desired CO methylation transition states that decreases activation barriers by ~25 kJ mol^{-1} relative to the $H_{12\text{-MR}}^{+}$ and prevents nucleophilic attack by molecules larger than CO (*e.g.*, DME or larger hydrocarbons) that lead to unproductive reaction events.[254,279] Further experimental studies and computational studies using dispersion-corrected DFT methods, higher-level quantum mechanics, or *ab initio* molecular dynamics support the findings that active sites within 8-MR voids of MOR,[280–283] FER,[118,284] CHA,[285] RRO,[286] ETL,[287] and SZR[288,289] zeolites selectively catalyze CO methylation to methyl acetate.

These studies highlight how kinetically controlled experiments alongside appropriately chosen theoretical models help to establish the identity, number and catalytic consequences of distinct H^+ ensembles and further motivate strategies to manipulate the active site environment for desired catalytic transformations. Such catalyst design strategies are enabled by synthetic placement of H^+ sites in desired voids *via* varying organic SDA structures (Section 2.1.1; shown in Fig. 10C for FER) or post-synthetic removal of H^+ sites in undesired voids *via* selective Na^+ exchange (Section 2.1.2; shown in Fig. 10B for MOR). Next, we show how the intrinsic selectivity among competing transition states sharing the same precursor state is biased by altering the active site environment for a fixed zeolite using synthetic protocols.

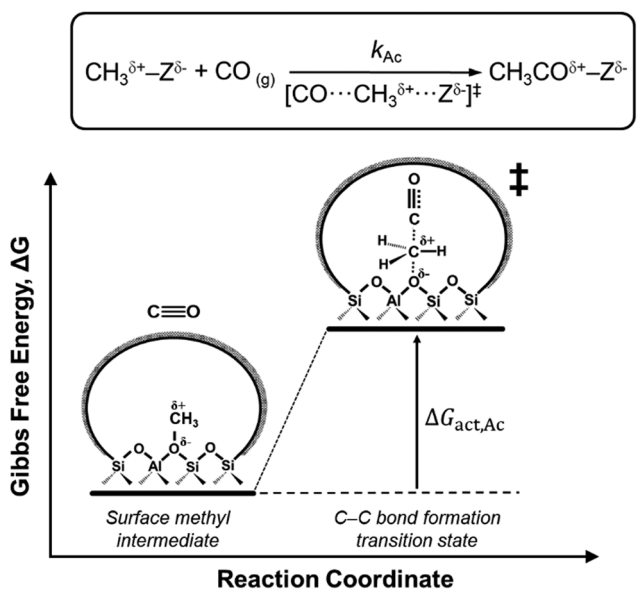

Fig. 11 Reaction coordinate diagram for CO methylation by a surface methyl species confined within zeolite voids. Adapted from Gounder *et al.*[39]

2.3.2. Preferential destabilization of bulkier transition states that share the same precursor state during toluene methylation in 10-MR of MFI and TON zeolites. Toluene methylation by DME or methanol is typically performed at high temperatures (573–773 K) on medium pore zeolites (*e.g.*, MFI) that have been designed to preferentially sieve *para*-xylene (*p*-X) over *ortho* and *meta* regioisomers (*o*-X, *m*-X) from their thermodynamic equilibrium distributions (~25% *p*-X, ~25% *o*-X, ~50% *m*-X; 573–673 K)[290] within micropores.[29,291–295] At 403 K, the xylene distribution on MFI zeolites synthesized using TPA^+ (MFI-TPA) reflects kinetic control by electrophilic aromatic substitution (~27% *p*-X, ~65% *o*-X, ~8% *m*-X) that is weakly influenced by the larger intersections that predominantly contain the H^+ sites in MFI-TPA;[131] such low-temperature conditions (<473 K) suppress the contributions of xylene isomerization reactions and intracrystalline diffusional constraints that promote *p*-X selectivity (>30%) at high temperatures.[29,131,293–295] In contrast, MFI zeolites synthesized using non-conventional SDAs (MFI-DABCO, MFI-EDA) exhibit altered isomer selectivities (~78% *p*-X, ~20% *o*-X, ~2% *m*-X; 403–433 K) that are independent of crystallite sizes (0.4–13 μm), toluene conversion (0.02–3.5%), reactant pressures, and methylating agent (DME or methanol).[131] The xylene formation rates ($r_{i\text{X}}$; per total H^+; 403 K) are invariant with DME pressure (25–66 kPa) and transition from first- to zero-order dependence in toluene pressure (P_{Toluene}, 0.05–8.8 kPa; Fig. 12A).[131] This kinetic behavior is described by a mechanism-derived rate expression (eqn (3)) containing the rate constant to form xylene isomer *i* ($k_{i\text{X}}$) and the equilibrium constant for toluene-C_1 coadsorption (K_{C}):

$$\frac{r_{i\text{X}}}{[\text{H}^+]} = \frac{k_{i\text{X}} K_{\text{C}} P_{\text{Toluene}}}{1 + K_{\text{C}} P_{\text{Toluene}}} \quad (3)$$

Here, $k_{i\text{X}}$ reflects the Gibbs free energy barrier $\Delta G_{\text{act},i\text{X}}$ for the C–C bond formation transition state relative to the co-adsorbed toluene-surface methyl precursor state (Fig. 13A) and accounts for the number of degenerate ring positions that form each xylene isomer ($n_{\text{C-C},i}$):[131]

$$k_{i\text{X}} = n_{\text{C-C},i} \frac{k_{\text{B}} T}{h} e^{\frac{-\Delta G_{\text{act},i\text{X}}}{RT}} \quad (4)$$

Rate constant ratios ($k_{i\text{X}}/k_{j\text{X}}$) are independent of the precursor state and reflect the Gibbs free energy difference between xylene formation transition states ($\Delta\Delta G_{i\text{X-}j\text{X}}$):[131]

$$\frac{k_{i\text{X}}}{k_{j\text{X}}} = \frac{n_{\text{C-C},i}}{n_{\text{C-C},j}} e^{\frac{-\Delta\Delta G_{i\text{X}-j\text{X}}}{RT}} \quad (5)$$

All three $k_{i\text{X}}$ values are lower (2–3× for *p*-X; 20–40× for *o*-X and *m*-X) on MFI-EDA and MFI-DABCO than on MFI-TPA. We apply the Hammond-Leffler postulate[296,297] to approximate relative transition state sizes from the xylene sizes (*p*-X, d_{kin} = 0.585 nm; *o*-X, *m*-X, d_{kin} = 0.68 nm) and propose that the differences in $k_{p\text{X}}/k_{o\text{X}}$ ratios on MFI-DABCO and MFI-EDA (~4–6) relative to that on MFI-TPA (0.4) reflect xylene formation transition state stabilities that are altered by a significant shift in the active

Open Access Article. Published on 20 September 2024. Downloaded on 1/24/2026 9:35:52 AM.
This article is licensed under a Creative Commons Attribution-NonCommercial 3.0 Unported Licence.

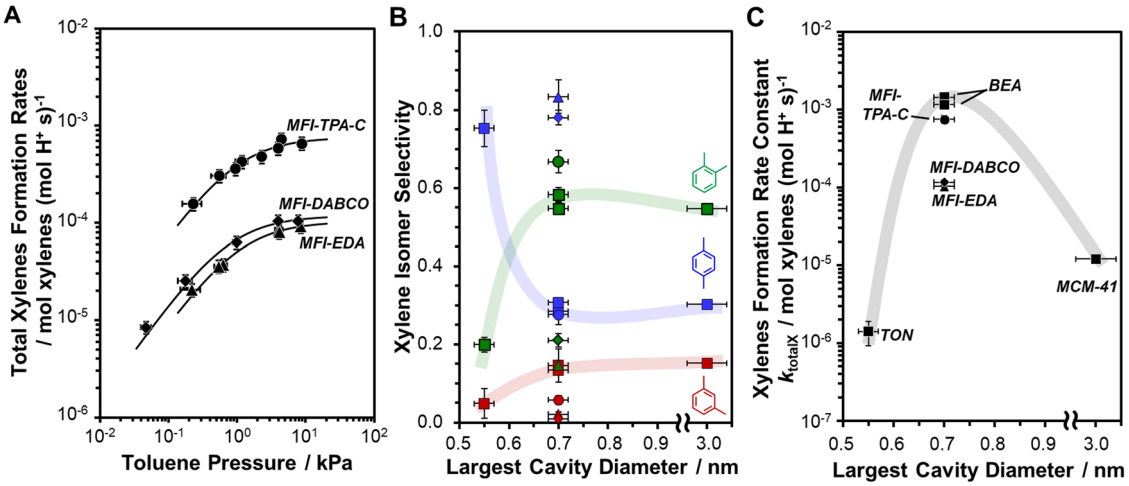

Fig. 12 (A) Total xylene formation rates as a function of toluene pressures during toluene methylation (403 K) by DME (66 kPa) on MFI zeolite samples (Si/Al ~ 50) synthesized using different organic SDA MFI-DABCO (◆), MFI-EDA (▲) and on a commercial MFI sample surmised to be synthesized using TPA (MFI-TPA-C (●)). Solid lines represent regressed best fits to eqn (3). (B) Average measured xylene isomer selectivity and (C) total xylene formation rate constant as a function of largest cavity diameter on aluminosilicates. Lines represent visual trends for non-MFI aluminosilicates (TON, BEA, MCM-41; ■) and serve to guide the eye. Adapted with permission from Ezenwa *et al.*[131] Copyright 2024 American Chemical Society.

environment of MFI towards the smaller channels;[131] such bias in active site environments results from the influence of organic SDA on Al siting (Section 2.1.1).

Relative DFT-calculated barriers for toluene methylation by surface methyls located at all 48 distinct O_f atoms show that MFI intersection environments similarly stabilize all three xylene formation transition states (average $\Delta\Delta G_{pX\text{-}oX,DFT}$ = 3 kJ mol^{-1}), while channel environments preferentially destabilize the bulkier transition states that form *o*-X and *m*-X (average $\Delta\Delta G_{pX\text{-}oX,DFT}$ = −22 kJ mol^{-1}) (Fig. 13B).[131] Furthermore, enthalpic contributions dominate these Gibbs free energy differences at low temperatures (403 K),[131] consistent with the functional form of the equation for Gibbs free energy where entropic losses upon confinement are less dominant.[265] Further kinetic and DFT analyses of additional microporous and mesoporous aluminosilicates containing uniform void sizes reveal that more constrained active site environments (~0.55 nm diameter) preferentially destabilize bulkier transition states, while more spacious active site environments (~0.70 nm diameter) similarly stabilize all isomer transition states relative to unconfined environments (~3.0 nm diameter) (Fig. 12B and C).[131]

These results highlight how the active site environment alters kinetically controlled reaction outcomes when competing

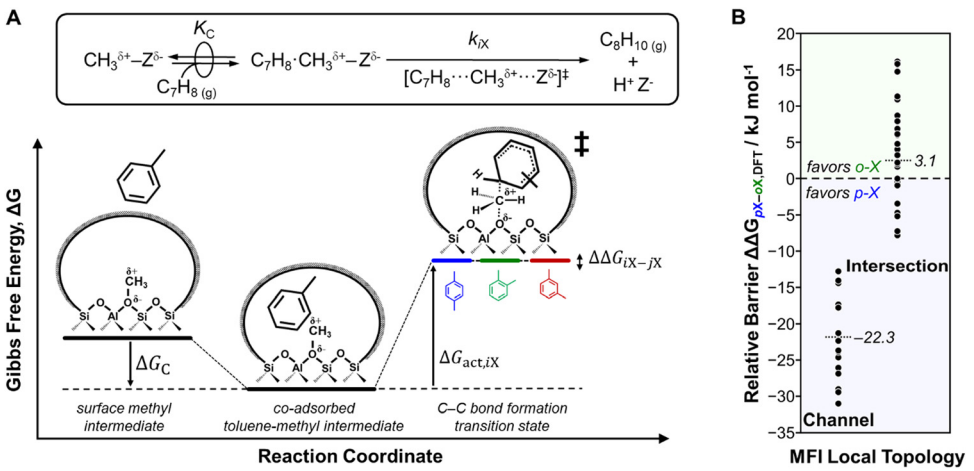

Fig. 13 (A) Gibbs free energy *versus* reaction coordinate diagram for toluene methylation to xylene on a confined Brønsted acid site showing that kinetic (k_{iX}) and thermodynamic (K_C) constants reflect the free energy barriers to form the toluene methylation transition states from co-adsorbed precursor states ($\Delta G_{act,iX}$) and the free energy difference between the co-adsorbed toluene-methyl intermediate and the surface methyl intermediate with toluene in the gas phase, respectively. Free energy differences between individual xylene formation transition states ($\Delta\Delta G_{iX-jX}$) are independent of the precursor state. Adapted with permission from Ezenwa *et al.*[131] Copyright 2024 American Chemical society (B) DFT-calculated $\Delta\Delta G_{pX-oX}$ for toluene methylation by surface methyls at all 48 T–O pairs in MFI organized by whether the O atoms are accessible to intersection or only accessible to straight or sinusoidal channels. Free energies are reported at 403 K, 1 bar. Reproduced with permission from Ezenwa *et al.*[131] Copyright 2024 American Chemical society.

 This journal is © The Royal Society of Chemistry 2024

Open Access Article. Published on 20 September 2024. Downloaded on 1/24/2026 9:35:52 AM. This article is licensed under a Creative Commons Attribution-NonCommercial 3.0 Unported Licence.

transition states have different sizes but share the same precursor state. These insights are further enabled by synthetic techniques that place active sites within distinct confining voids of MFI zeolites. Such active site design strategies complement design strategies that deactivate active sites in unselective pore environments in MWW zeolites for toluene methylation (623 K)[30,31] and crystallite design approaches that promote the preferential sieving of the faster diffusing *p*-X isomer.[29,293–295] Furthermore, this active site design approach adds to the growing toolbox of approaches[298–301] that aim to design zeolites that contain active site scaffolds which stabilize desired transition states and reactive intermediates for a given reaction.[302]

3. Active sites at external crystallite surfaces or mesopore environments

In Section 2, we discussed synthesis–structure–reactivity relationships for location of Al (and associated H^+) within distinct confining environments (0.4–2.0 nm diameter) of internal micropores. Here in Section 3, we focus on the location of Al (and H^+) at unconfined environments (>2.0 nm diameter) of external crystallite surfaces or mesopores that are directly connected to external surfaces (Fig. 14). Our discussion excludes H^+ sites that are located within mesopores accessible only from intracrystalline micropore regions (Fig. 14) as such sites possess the limited accessibility of internal sites that excludes certain bulky molecules and the reactivity of external sites with environments that are unable to confine certain reactive intermediates and transition states. We examine synthetic and post-synthetic strategies to control the number of external acid sites in zeolite and present experimental and computational approaches to characterize external acid sites. We further briefly mention a few examples where external active sites have been proposed to influence catalysis. Although we highlight various zeolites, we focus more of the examples in this section on MFI zeolites which are used widely in industrial catalytic applications and are often representative of the broader family of medium pore zeolites possessing limiting apertures that hinder the accessibility of bulk molecules to internal H^+ sites.

3.1. Synthetic and post-synthetic strategies to manipulate the number of external acid sites

The number of external H^+ sites on a zeolite depends on various crystallite-scale properties including the crystallite size and morphology, the bulk H^+ content, and the spatial Al concentration (also known as zoning). Synthetic or post-synthetic techniques that alter these bulk properties, without unintended effects to the number or distribution of internal H^+ sites, offer strategies to independently tune the number of external H^+ sites and the internal H^+ distribution (Fig. 15).

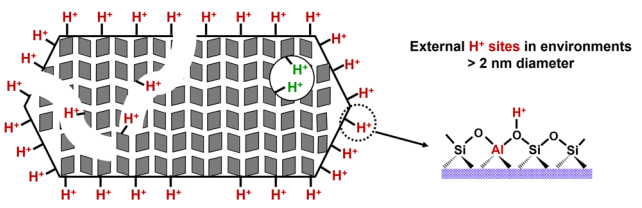

Fig. 14 Schematic depicting location of H^+ sites at external surfaces and mesopores that are directly connected to external surfaces. H^+ sites located within mesopores that are only accessible from internal micropore regions are shown in green.

3.1.1. Controlling crystal size and morphology. Assuming a homogenous concentration of framework Al and associated H^+ across the crystallite length (H^+ atoms per nm), the number of external H^+ sites for a zeolite sample can be reasonably estimated from knowledge of the framework density of T-atoms (per unit cell volume), the bulk H^+ density (per number of T-atoms), and the crystallite size and morphology. Such estimations also require approximating the often-irregular shapes of zeolite crystallites as spheres, cylinders, or rectangular slabs. This indicates that the ratio of external H^+ sites to total H^+ sites is proportional to the surface area-to-volume ratio, which in turn is inversely proportional to the characteristic length of the assumed crystal morphology (*e.g.*, radius for spheres). Expressions for the fraction of external H^+ sites as a function of average crystallite radius have been reported by Farcasiu and Degnan[303] for FAU zeolites and by Gilson and Derouane[304] for MFI zeolites.

Synthetic and post-synthetic approaches to tune the crystallite size, morphology, and architecture have been developed for certain zeolites and fall under the realm of crystal engineering, which manipulates the factors (*e.g.*, temperature, pH, identity and concentration of inorganic and organic precursors, seeds, growth modifiers) that control the mechanism and rates of crystal nucleation, growth, and dissolution.[69,103,107] Such approaches to produce zeolites possessing nanosized morphologies (*e.g.*, nanoparticles, two-dimensional or layered, or surfaces modified with protrusions or fins) or hierarchical architectures (*e.g.*, pillared, mesoporous) have been summarized by comprehensive reviews and perspectives in the past decade[62–75] and will not be discussed here. However, modifying the crystal size and morphology alters the diffusion path length and, in some cases, the effective diffusivity of a molecule in a given framework. Nevertheless, tuning the crystallite size and morphology *via* synthetic or post-synthetic approaches provides an indirect approach to manipulate the number of external H^+ sites (relative to total H^+ sites) for a given zeolite framework at fixed total H^+ content.

3.1.2. Inducing Si and Al zoning during synthesis. Since early reports[305–310] of non-homogenous concentrations of Al across the crystallite length of zeolites, numerous subsequent studies[311–329] (mostly on MFI) have further confirmed that spatial concentration gradients of Al and Si can exist. Elemental zoning phenomena result in external crystallite surfaces that have significantly higher or lower Si/Al ratios than the bulk zeolite. Although the mechanisms of elemental zoning during zeolite synthesis are not yet fully understood, they are generally proposed to reflect differences in the relative rates of incorporation of Si and Al precursors from the synthesis gel into the growing crystal, which in turn depends on various factors during zeolite synthesis such as precursor sources,

Open Access Article. Published on 20 September 2024. Downloaded on 1/24/2026 9:35:52 AM.
This article is licensed under a Creative Commons Attribution-NonCommercial 3.0 Unported Licence.

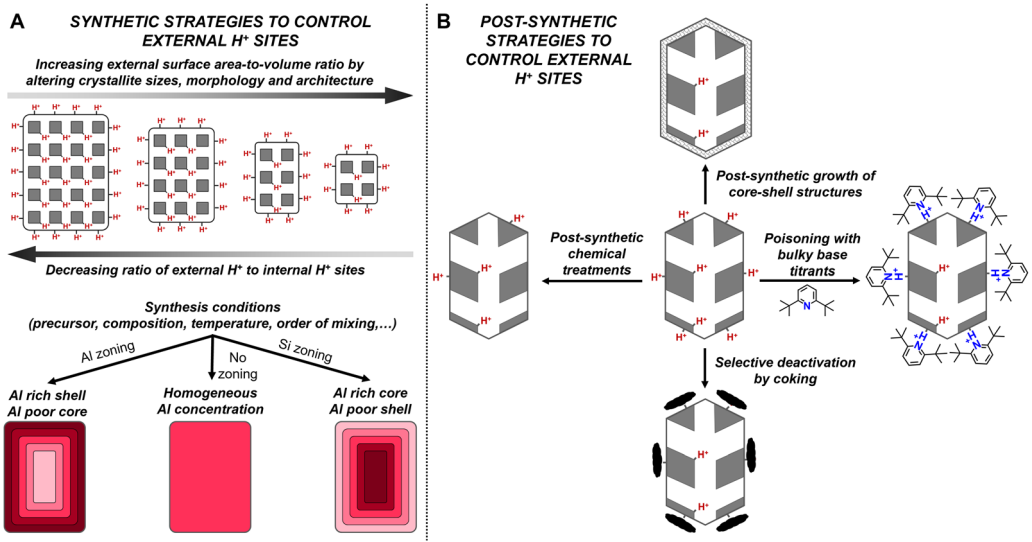

Fig. 15 Summary of highlighted synthetic and post-synthetic techniques to control the number of external H^+ sites.

temperature, order of mixing, and aging.[313–317,323–328] Further discussion on elemental zoning can be found in recent reviews.[83,84] Thus, adapting reported synthetic protocols that induce Si and Al zoning may offer an approach to vary the external H^+ content relative to bulk H^+ content.

3.1.3. Post-synthetic coating with crystalline or amorphous silicate shells. The secondary growth or deposition of thin silicate or aluminosilicate layers (*i.e.*, shells) on the external surfaces of zeolite crystallites (*i.e.*, cores) results in core@shell zeolite architectures where the number of external H^+ sites is controlled by the H^+ content of the shell.[67,84] More commonly, crystalline Al-free shells (*e.g.*, Si-MFI) are grown over the Al-containing core (*e.g.*, Al-MFI) in aqueous growth media to create surface passivated core@shell structures of the same framework type (*e.g.*, Al-MFI@Si-MFI)[330–334] or different framework composites (*e.g.*, Al-BEA@Si-MFI).[335–338] Such techniques require an epitaxial shell growth to limit pore blockage because misaligned lattices can hinder molecular diffusion through the crystallite.[84,339–341] Furthermore, chemical vapor or liquid deposition (CVD or CLD) of silicon based compounds (*e.g.*, organosilanes, silicon alkoxides) followed by high-temperature treatments in dioxygen is often used to grow amorphous silica oxide domains on external crystallite surfaces, which passivate the external H^+ sites.[52,342–351] These various techniques to coat crystallites with crystalline or amorphous silica layers provide opportunities to tune the number of external H^+ sites, but may also alter molecular diffusion behavior to enter or traverse intracrystalline micropores.

3.1.4. Post-synthetic chemical treatments. Post-synthetic chemical treatments of zeolites have been reported to passivate external acid sites in various frameworks (*e.g.*, MFI, MOR, FAU, FER). Mild chemical treatments using aqueous solutions of ammonium hexafluorosilicate (AHFS),[190,352–360] oxalic acid,[361–364] ethylenediaminetetraacetic acid (EDTA),[365] or nitric acid[366,367] have been reported to preferentially remove external Al atoms (and associated H^+ sites in the case of framework Al); such treatments (especially AHFS) are also known to preferentially remove extra-framework Al or partially-coordinated framework Al species.[368–373] Treatments of MFI zeolites with $SiCl_4$ vapors have also been reported to preferentially replace external Al atoms with Si atoms.[374,375] We recently reported that the treatment of MFI zeolites with multiple AHFS cycles results in a progressive decrease in the number of external H^+ sites (up to 99% removal efficacy) with negligible changes (<10%) to the bulk H^+ content.[376] Although the mechanism of selective external acid site removal during chemical treatments has not yet been established, mild chemical treatments of zeolites remain a promising route to alter the number of H^+ sites on the external crystallite surfaces.

3.1.5. Poisoning with bulky base titrants. Large base titrants (*e.g.*, 2,4-dimethylquinoline, d_{kin} ~ 0.90 nm; 2,6-di-*tert*-butylpyridine (DTBP), d_{kin} ~ 0.80 nm; 2,4,6-trimethylpyridine, d_{kin} ~ 0.70 nm) selectively poison external H^+ sites in medium-pore zeolites (*e.g.*, MFI, MTT) whose limiting apertures (~0.55 nm) restrict the access of such bulky bases to internal H^+ sites.[30,347,377–386] For large pore zeolites (*e.g.*, FAU, BEA) with larger pore apertures (~0.70 nm), even bulkier base titrants (*e.g.*, 2,4,6-tri-*tert*-butylpyridine (TTBP), triphenylphosphine oxide, d_{kin} ~ 1.1 nm) are often needed to selectively titrate external H^+ sites.[245,387,388] Typically, during catalysis, these base titrants are introduced to the zeolite before the reactant to irreversibly poison external H^+ sites prior to reaction, or co-fed with reactants, especially in cases where external H^+ sites are reversibly poisoned by the base titrant. These highlight that poisoning by bulky base titrants is an approach to control the number of external H^+ sites on a zeolite sample.

3.1.6. Selective deactivation by coking. External H^+ sites are routinely implicated in the unrestricted formation of bulky polyaromatic species that are precursors to coke.[52,332,375,389–391] In some cases, the selective deactivation (“selectivation”) of external H^+ sites by coking has been observed for some medium pore zeolites such as MFI, MWW, MTT.[194,196,392–395] Although

 This journal is © The Royal Society of Chemistry 2024

Open Access Article. Published on 20 September 2024. Downloaded on 1/24/2026 9:35:52 AM. This article is licensed under a Creative Commons Attribution-NonCommercial 3.0 Unported Licence.

the accessibility of internal H^+ sites may be hindered by pore-blocking species on the external surface, this selective coking behavior has provided a strategy to passivate external H^+ sites either by catalyst pre-coking before the reaction or by *in situ* coking during the reaction.

3.2. Characterization of active site locations at external surfaces

External H^+ sites charge compensate $[AlO_{4/2}]^-$ tetrahedra that are structurally similar to those located within microporous voids. Computational studies that correct for systematic artifacts of periodic DFT methods have shown that the ensemble averaged DPE of H^+ sites at all isolated Al locations across different zeolite frameworks (MFI, BEA, FER, MOR, CHA, FAU; 1201 ± 11 kJ mol^{-1}) are similar to those of H^+ sites at the unconfined surfaces of mesoporous aluminosilicates (Al-MCM-41; 1212 kJ mol^{-1}).[7,8] Recent DFT studies for MFI zeolites have further shown that the ensemble averaged DPE of most external H^+ sites are similar to those of internal H^+ sites, except for the minority of Brønsted acid sites originating from an H_2O molecule coordinating to a trigonal planar Al site that substitutes an external silanol.[10] Together, these studies indicate that the strength of Brønsted acid sites is independent of confining void environment. However, external H^+ sites differ from internal H^+ sites in the inability of unconfined surfaces to restrict the access or formation of bulky species and to provide effective van der Waals stabilization of reactive intermediates and transition states. Thus, techniques to quantify the number of external H^+ sites on zeolites mostly depend on the use of stoichiometric probes that selectively titrate only external H^+ sites or the use of catalytic probes that exclusively react at external H^+ sites.

Bulk characterization techniques for Al atoms in zeolites (*e.g.*, elemental analysis, ^{27}Al NMR) are unable to distinguish Al atoms located at surface locations *versus* interior locations of the zeolite crystallite. As a surface sensitive technique, X-ray photoelectron spectroscopy (XPS) probes the relative Si and Al contents of the crystallite surface and provides useful insights into the presence of spatial concentration gradients of Si and Al atoms across the crystallite length scale,[304–306,358,374,380] especially when coupled with depth profiling techniques.[320,322,341] However, estimating the number of external H^+ sites in zeolites *via* XPS remains qualitative because XPS provides spatially averaged information of the exterior region of the crystallites (up to 10 nm depth) and requires the assumption that all surface Al are in framework positions and are associated with a proton. Furthermore, low XPS signal-to-noise ratios for zeolite samples containing surface Si/Al > 100 further preclude the use of XPS to reliably estimate the number of external acid sites.[339] Nevertheless, XPS provides an approach to assess when the number of external H^+ sites deviates significantly from that expected from a homogeneous distribution of H^+ across the crystallite.

Bulky base molecules (described in Section 3.1.5) are used to selectively titrate external acid sites over internal H^+ sites.[380] Quantifying the number of external H^+ sites requires knowledge of binding stoichiometry (often 1 : 1 titrant : H^+) and that chemisorbed titrants on external Brønsted acid sites can be distinguished from chemisorbed titrants on external Lewis acid sites and physisorbed titrants on external surfaces and mesopores.[237,380,383,396] Distinct IR and NMR spectroscopic signatures for chemisorbed titrants on external Brønsted acid sites can be used to distinguish different adsorbed titrants.[245,255,384,397–399] Furthermore, alkylpyridine bases containing sterically hindered N centers (*e.g.*, DTBP, TTBP) are unable to coordinate with Lewis acidic Al centers;[380,396,400] such features allow certain hindered bases to be used to quantify external H^+ sites *in situ* during steady-state reactions or *ex situ* using thermogravimetric and temperature-programmed desorption techniques.[376,401–403] Together, these highlight how bulky base titrants can be used to quantify the number of external H^+ sites in zeolites. However, reliable quantification using stoichiometric probes is limited to samples containing significant amounts of external H^+ sites (>10 μmol external H^+ g^{-1}), because of typical equipment detection limits.[339,376,380,396]

Catalytic reactions that react solely on external H^+ sites can serve as a probe to quantify the number of external H^+ sites in a given zeolite. Various catalytic probe reactions for external H^+ sites, mostly in medium-pore zeolites, have been explored over the history of zeolite catalysis and usually involve reactions of bulky aromatic molecules.[403,404] The gas-phase cracking of 1,3,5-triisopropylbenzene (d_{kin} ~ 0.90 nm)[334,339,374,380,402] and the liquid-phase benzylation of 1,3,5-trimethylbenzene (mesitylene; d_{kin} ~ 0.70 nm)[381,405–409] are two reactions that are routinely employed in comparative assessments of the number of external H^+ sites across medium pore zeolites (typically MFI). Regardless of the choice of a reaction, a quantitative kinetic probe of external H^+ sites requires that it solely reflects the concentration of reactive intermediates and kinetically relevant transition states; such requirements can be fulfilled by operating at conditions where measured rates are (i) kinetically controlled without influences of extracrystalline transport restrictions, (ii) in a fixed kinetic regime, preferably first- or zero-order dependence on reactant pressures, (iii) not convoluted by side reactions and deactivation, and (iv) not influenced by approach to equilibrium artifacts. Quantitative kinetic probes for external H^+ sites can be further validated using samples containing external H^+ sites that can be reliably quantified using a stoichiometric probe (*e.g.*, DTBP titration).[381] We demonstrated these in our recent report[376] where we developed mesitylene benzylation by dibenzyl ether as a kinetic method to quantify external H^+ sites in MFI zeolites obtained after surface passivation treatments (Fig. 16). Catalytic probes, when compared to stoichiometric probes, provide an active site quantification method that amplifies dilute concentrations of external H^+ sites, thereby allowing more reliable assessments when the number of external H^+ sites is below the detection limits of conventional techniques. Furthermore, these kinetic methods are positioned to advance studies that aim to develop rigorous (post)synthesis–structure–reactivity relationships for external H^+ sites during acid catalysis.

Open Access Article. Published on 20 September 2024. Downloaded on 1/24/2026 9:35:52 AM.
This article is licensed under a Creative Commons Attribution-NonCommercial 3.0 Unported Licence.

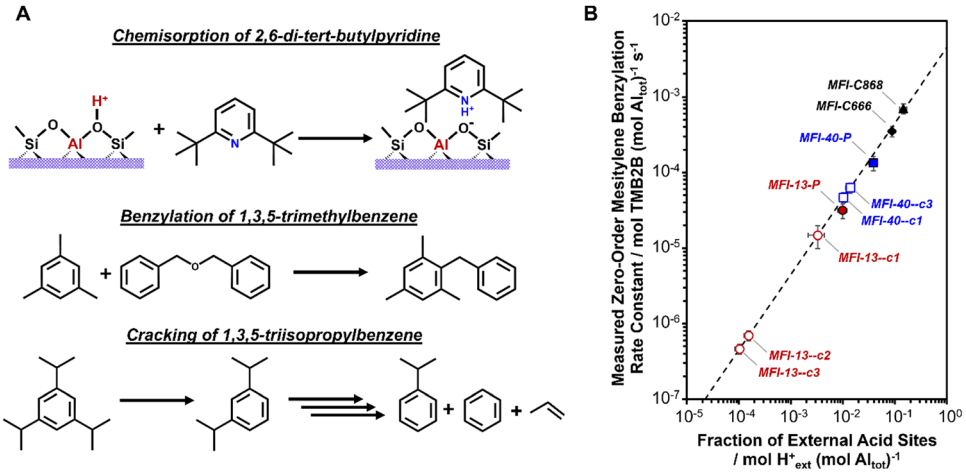

Fig. 16 (A) Some stoichiometric and catalytic probes used to assess external H^+ sites. (B) Dependence of mesitylene benzylation rates per g on the number of external H^+ sites per g zeolite. Measured zero-order rate constants (per total Al) for mesitylene benzylation with DBE (363 K) as a function of fraction of external H^+ sites (per total Al) on MFI-13-P (●), MFI-40-P (■), MFI-C666 (◆) and MFI-C868 (▲). The intrinsic mesitylene benzylation rate constant was further used to estimate the fraction of external H^+ sites on samples post-synthetically modified with AHFS in multiple treatment cycles (open symbols). Adapted with permission from Ezenwa *et al.*[376] Copyright 2024 Royal Society of Chemistry.

3.3. Catalytic consequences of active sites at external unconfined surfaces

External H^+ sites in zeolites have been reported to influence reactivity, selectivity and deactivation behavior during Brønsted acid catalysis, especially under conditions where intracrystalline diffusion constraints restrict access and egress from internal H^+ sites. For toluene methylation under kinetically controlled conditions (403 K), external H^+ sites exhibit xylene selectivity (*o*-X ~ 60%, *p*-X ~ 30%, *m*-X ~ 10%) similar to that of internal H^+ sites at MFI intersections but rates that are $\sim 10^2\times$ lower than those of H^+ sites at MFI intersections.[131] In contrast, earlier toluene methylation studies at higher temperatures (573–773 K) reported that external H^+ sites in MFI zeolites alter diffusion controlled selectivity (*p*-X ~ 99%) towards thermodynamic equilibrium (*o*-X ~ 25%, *p*-X ~ 25%, *m*-X ~ 50%) by allowing xylene isomerization *via* bulky transition states that are hindered within micropores.[292,334,379,410,411] External H^+ sites were also reported to affect oligomer selectivity during propene oligomerization (463–523) in medium pore zeolites (MFI, MTT, TON)[359,385,386] and accelerate coke deposition rates on external surfaces during methanol-to-hydrocarbons (743 K) in MFI zeolites.[390] Further analysis of the catalytic consequences of external H^+ sites is beyond the scope of this perspective.

4. Outlook and conclusions: designing active site environments in Brønsted acid zeolites

Catalytic reactions mediated by Brønsted acid zeolites are influenced by the sizes and shapes of the void environments that confine active H^+ sites and of the intermediates and transition states stabilized at such sites. In Sections 2 and 3, we presented synthesis–structure–reactivity relationships for active site environments in zeolite catalysis. We discussed how synthetic or post-synthetic approaches can be used to selectively place or remove protons in distinct void environments of given zeolite framework and highlighted characterization strategies that can be used to identify and quantify the location of H^+ sites (or framework Al) within distinct void environments (or lattice positions). We further discussed how active site environment influences reactivity and selectivity during catalysis under kinetically controlled conditions. Despite advances in the design of active site environments in zeolites, several challenges remain that present hurdles in our ability to precisely (i) control the location, (ii) identify and quantify the number, and (iii) elucidate the catalytic consequences of active sites in distinct void environments. Here in Section 4, we highlight research opportunities to address knowledge gaps that hinder more precise control and understanding of active site environments in Brønsted acid zeolite catalysis.

4.1. Controlling the location of active sites within distinct environments

The framework Al siting in a given zeolite depends on the relative rates and stabilities of Al incorporation at various lattice positions, which in turn depend on the crystallization conditions such as identity and quantity of Si or Al precursors and the SDAs.[46,87] Thus, efforts to understand the various interactions between SDAs and the inorganic zeolite framework will aid in clarifying the factors influencing the location and orientation of SDAs within distinct voids features.[119,149,171,412–422] The ability to control the location of active sites within distinct void environments will benefit from efforts to deconvolute the effects of structure and mobility of organic SDAs on their interactions with framework Al centers.[171,172,419] Even after completion of bulk crystallization,

 This journal is © The Royal Society of Chemistry 2024

Open Access Article. Published on 20 September 2024. Downloaded on 1/24/2026 9:35:52 AM. This article is licensed under a Creative Commons Attribution-NonCommercial 3.0 Unported Licence.

framework Al atoms can be redistributed because of reversible cleavage and formation of Si–O–Al bonds; such Al rearrangements are affected by various factors including crystallization times, temperatures, and SDAs.[423–426] Delineating how the temporal Al distribution depends on kinetic control (*i.e.*, dictated by relative rates of Al incorporation among various T-sites) *versus* thermodynamic control (*i.e.*, dictated by relative stabilities of Al incorporated at various T-sites) remains challenging,[87] but is important to further clarify when and how organic SDAs bias the siting of Al centers at various lattice positions.

Although the exclusion of bulky base titrants from protons in smaller voids of certain zeolite frameworks can be explained using size-exclusion arguments,[174,185–187] the ability of smaller cations (*e.g.*, Na^+) to preferentially exchange certain proton ensembles,[11,13,182–185] despite their accessibility to all distinct void environments, requires further insights into the intermolecular interactions that dictate such behavior. Molecular-level descriptions of how active sites in distinct confining environments[30,192,193,195,198] or at unconfined zeolite surfaces[52,332,375,389–391,427] deactivate during catalysis will enable strategies to harness the selective deposition of unreactive residues in tuning active site environments in zeolites. Further insights are needed into the effects of post-synthetic treatment conditions on selective removal of Al atoms from certain T-sites or from external crystallite surfaces[373,428,429] and on the selective re-insertion of Al atoms into certain vacancy defects following the removal of relatively unreactive heteroatoms (*e.g.*, B). These efforts to develop deeper insights into the effects of post-synthetic treatments on the selective removal of active sites in undesired void environments will complement the efforts to elucidate the effects of synthetic parameters on the selective placement of active sites in desired environments.

4.2. Identifying and quantifying active sites in distinct void environments

Further advances in ^{27}Al NMR techniques[180,220,226,227,430] may enable researchers to more precisely and unambiguously resolve spectroscopic signals for certain zeolite frameworks (*e.g.*, MFI, MWW) into their contributions from distinct framework Al lattice positions. Identifying the highest probability locations of Al atoms in zeolites will also benefit from further advances in XRD techniques[119,120,124,230,232] and multinuclear and multidimensional NMR techniques[179,180,220,416,431] that probe the location and orientation of organic SDA molecules within voids and their interaction with framework Al centers. Studies to identify probe molecules with distinct spectroscopic (*e.g.*, NMR, IR) signatures when adsorbed at protons or cations within different zeolite void environments could also offer an approach to quantify distinct H^+ environments. Emerging techniques such as integrated differential phase contrast scanning transmission electron microscopy (iDPC-STEM)[432–435] allow imaging distinct atomic positions of heteroatoms substituted within zeolite frameworks and the orientations of base titrants (*e.g.*, pyridine) within zeolite pores. Substituting lighter N atoms ($Z = 7$) in base titrants with heavier atoms such as S ($Z = 16$)[433] and framework Al atoms ($Z = 13$) with heavier heteroatoms such as Ti ($Z = 22$) or In ($Z = 49$) may make it possible to use iDPC-STEM, to better resolve atomic positions in the organic guests and zeolite hosts, respectively. Ultimately, advancements in the identification and quantification of distinct Al (and H^+) environments will bolster efforts to control the active site environments and to distinguish the intrinsic reactivity of active sites within distinct environments.

4.3. Elucidating effects of active site environments on catalysis

Clarifying the effects of active site environments on catalysis requires maintaining the link between reactivity and local environment of active sites and bound species;[38,39] this requires that effects of thermodynamics, transport, and deactivation, often present in experimentally measured data, are eliminated or accounted for in the development of kinetic models and in mechanistic interpretations.[16,18,19,27,77,131,268,436–438] Thus, efforts to vary the active site environment at fixed bulk zeolite property (*e.g.*, crystallite sizes, active site density) and *vice versa*,[75,200,436,439] and to measure intrinsic diffusional properties (*e.g.*, D/R^2)[268,436,440,441] may permit the deconvolution of transport effects from intrinsic kinetics at distinct active site environments. When possible, the contributions of external H^+ sites to observed reactivity and selectivity should be distinguished from those of internal H^+ sites; these contributions depend on the number and reactivity of external H^+ sites (relative to internal H^+ sites).[10,303] Furthermore, techniques to quantify active site ensembles *via* spectroscopic or titrimetric methods during catalysis are preferable over *ex situ* techniques that may overestimate the number of catalytically active protons; such techniques also facilitate rigorous assignments of differences in measured turnover rates to the free energy differences between kinetically relevant transition states and reactive intermediates.[44,257,442,443]

The reactions of hydrocarbons (*e.g.*, alkene oligomerization and arene methylation) and oxygenates (*e.g.*, methanol/DME to hydrocarbons) in zeolites often involve complex reaction networks containing $\sim 10^2$–10^4 constituent reactions.[16,444–446] The nature of such complex reactions create challenges in elucidating effects of active site environments on catalytic reactivity and selectivity. Where possible, isolated constituent reactions or reaction conditions such as lower temperature and conversions that simplify complex networks ($<10^1$ reactions) allow more facile connections between measured kinetic and thermodynamic constants to the energetics of specific elementary steps in reaction mechanisms. Continued endeavors to explore catalytic reactions that are sensitive to active site environments, including reaction chemistries of industrial relevance, will enable developing quantitative catalytic probes for distinct active site environments.

Catalysis remains the ultimate arbitrer of differences in active site environments, because under kinetically controlled conditions, reactivity and selectivity differences reflect ensemble averaged reactive encounters with active sites. Thus, the aforementioned experimental efforts to control and quantify active site environments and elucidate their effects on catalysis

Open Access Article. Published on 20 September 2024. Downloaded on 1/24/2026 9:35:52 AM. This article is licensed under a Creative Commons Attribution-NonCommercial 3.0 Unported Licence.

will be supported by the ensuing theoretical efforts to develop molecular insights into synthesis–structure–reactivity relationships for active site environments in Brønsted acid zeolites.

4.4. Advancing computational approaches to interrogate the synthetic placement and catalytic consequences of distinct Al locations and H^+ environments

The vast compositional space encountered during zeolite synthesis will benefit from data-driven approaches to catalogue synthesis information from literature, analyze results from high-throughput experimentations and simulations, and decompose complex synthesis phenomena into tractable descriptors that capture how synthesis parameters regulate Al siting.[419,447–456] Such approaches also permit the rapid screening of large numbers of known or hypothetical organic SDAs against all Al locations in a given zeolite to identify promising candidates for further studies using more accurate theoretical simulations.[457] The design of zeolites that contain active site environments which stabilize desired transition states and reactive intermediates of a given reaction offers an approach to directly link synthesis to reactivity.[298–302] This approach is aided by theoretical calculations and computational screening workflows that assist in identification of organic SDAs that resemble desired transition states or intermediates and candidate zeolites with active environments that stabilize these bound species.[298–302] Further advances in designing zeolites *via* organic SDA mimics may further uncover key features of active site environments that stabilize organic SDAs during synthesis and transition states or intermediates during catalysis.

The use of theoretical methods that account for dispersion forces is necessary for describing the effects of active site environment on the stabilities of intermediates and transition states.[39,44] In addition, studies that sample the locations of reactive intermediates and transition states across all possible Al and H^+ sites provide more insights than those that model only one or two Al lattice positions in lower symmetry frameworks.[131] Although such exhaustive approaches are computationally demanding, they are important for comparisons to experiments especially when adjudicating among competing hypotheses on the origins of diverse catalytic behavior for samples whose actual Al distributions are imprecisely known. Macroscopic properties (*e.g.*, kinetic and thermodynamic constants) are typically estimated from statistical averaging of microscopic free energies across all possible Al and H^+ locations. However, because the distributions of Al and H^+ sites are non-random and often unknown, care should be taken to ensure that theoretical calculations are appropriately used to interpret experimental results. Further advancements in molecular descriptions of catalysis in confined spaces can be achieved by replacing static size descriptors of voids (*e.g.*, PLD, LCD) and bound species (*e.g.*, kinetic diameter,[458,459] critical diameter,[459–461] van der Waals diameter[8,43,268,462]) with descriptors such as van der Waals interaction energies that account for the size and shape of non-spherical voids that dynamically restructure to maximize contacts with confined intermediates and transition states.[32,43,44,268,463]

In summary, further advances in the design of active site environments in zeolites for catalysis will continue to require closely integrated experimental and theoretical approaches to improve fundamental understanding of the molecular-level details that underlie synthesis–structure–reactivity relationships. Zeolites remain one of the most widely used industrial catalysts as Brønsted acids when substituted with trivalent heteroatoms (*e.g.*, Al^{3+}, B^{3+}), as Lewis acids when substituted with electron-deficient tetravalent heteroatoms (*e.g.*, Sn^{4+}, Ti^{4+}, Hf^{4+}), as supports for metal ions (M^{n+}) and complexes ($[M_xO_y]^{n+}$), or in bifunctional formulations with metal nanoparticles and clusters (*e.g.*, Pt). Thus, the ability to precisely place framework heteroatoms in zeolites, especially among the few frameworks ($\sim$10) that have already been scaled up and implemented for commercial applications, will have significant implications for the wide variety of reactions useful in upgrading traditional fossil feedstocks (*e.g.*, crude oil, shale gas) and emerging feedstocks (*e.g.*, biomass, waste plastics, CO_2) to higher value chemicals and fuels.

Data availability

No primary research results, software or code have been included and no new data were generated or analysed as part of this review.

Conflicts of interest

The authors declare that they have no known competing financial interests or personal relationships that could have appeared to influence work reported in this paper.

Acknowledgements

We acknowledge many former researchers at Purdue, including Dr Phil Kester, Dr Young Gul Hur, Dr Claire Nimlos, and Dr Byung Jin Lee for their technical and conceptual contributions to the findings described in this feature article and in previously published manuscripts related to controlling the distribution of H^+ sites in MFI zeolites. We thank Geoff Hopping, Eric Sauer, Savanna Mack, Teah Scott and Olivia Gluth for their contributions and helpful discussions on various aspects of external H^+ sites in MFI zeolites. We acknowledge Prof. David Hibbitts (Univ. of Florida), Dr Alexander Hoffman (Univ. of Florida), Hansel Montalvo-Castro (Univ. of Florida), Dr Deng-Yang Jan (Honeywell UOP), Prof. Bradley Chmelka (Univ. of California Santa Barbara), and Dr Michael Schmithorst (Univ. of California Santa Barbara) for their collaborations and contributions to the findings jointly published and discussed herein. We also acknowledge Andrew Norfleet and Ricem Diaz Arroyo for helpful technical discussions and for careful proofreading of this manuscript. The authors acknowledge financial support provided by the National Science Foundation under

 This journal is © The Royal Society of Chemistry 2024

Open Access Article. Published on 20 September 2024. Downloaded on 1/24/2026 9:35:52 AM. This article is licensed under a Creative Commons Attribution-NonCommercial 3.0 Unported Licence.

Cooperative Agreement No. EEC-1647722, which is an Engineering Research Center for the Innovative and Strategic Transformation of Alkane Resources. S. E. also acknowledges financial support from CISTAR Bill Murray and Dick Reitz Purdue Fellowships.

References

1 T. F. Degnan, in *Studies in Surface Science and Catalysis*, ed. R. Xu, Z. Gao, J. Chen and W. Yan, Elsevier, 2007, vol. 170, pp. 54–65.
2 W. Vermeiren and J.-P. Gilson, *Top. Catal.*, 2009, **52**, 1131–1161.
3 S. I. Zones, *Microporous Mesoporous Mater.*, 2011, **144**, 1–8.
4 C. Martínez and A. Corma, *Coord. Chem. Rev.*, 2011, **255**, 1558–1580.
5 W. O. Haag, R. M. Lago and P. B. Weisz, *Nature*, 1984, **309**, 589.
6 W. O. Haag, in *Studies in Surface Science and Catalysis*, ed. J. Weitkamp, H. G. Karge, H. Pfeifer and W. Hölderich, Elsevier, 1994, vol. 84, pp. 1375–1394.
7 A. J. Jones and E. Iglesia, *ACS Catal.*, 2015, **5**, 5741–5755.
8 S. Wang and E. Iglesia, *ACS Catal.*, 2016, **6**, 7664–7684.
9 M. Rybicki and J. Sauer, *Catal. Today*, 2019, **323**, 86–93.
10 H. Balcom, A. J. Hoffman, H. Locht and D. Hibbitts, *ACS Catal.*, 2023, **13**, 4470–4487.
11 R. Gounder and E. Iglesia, *J. Am. Chem. Soc.*, 2009, **131**, 1958–1971.
12 C. Song, Y. Chu, M. Wang, H. Shi, L. Zhao, X. Guo, W. Yang, J. Shen, N. Xue, L. Peng and W. Ding, *J. Catal.*, 2017, **349**, 163–174.
13 P. M. Kester, J. T. Crum, S. Li, W. F. Schneider and R. Gounder, *J. Catal.*, 2021, **395**, 210–226.
14 M. Guisnet and P. Magnoux, *Appl. Catal.*, 1989, **54**, 1–27.
15 P. M. Kester, E. Iglesia and R. Gounder, *J. Phys. Chem. C*, 2020, **124**, 15839–15855.
16 M. L. Sarazen, E. Doskocil and E. Iglesia, *ACS Catal.*, 2016, **6**, 7059–7070.
17 M. L. Sarazen, E. Doskocil and E. Iglesia, *J. Catal.*, 2016, **344**, 553–569.
18 E. E. Bickel and R. Gounder, *JACS Au*, 2022, **2**, 2585–2595.
19 E. E. Bickel, S. Lee and R. Gounder, *ACS Catal.*, 2023, **13**, 1257–1269.
20 R. Gounder and E. Iglesia, *J. Catal.*, 2011, **277**, 36–45.
21 A. J. Jones, S. I. Zones and E. Iglesia, *J. Phys. Chem. C*, 2014, **118**, 17787–17800.
22 J. R. Di Iorio, C. T. Nimlos and R. Gounder, *ACS Catal.*, 2017, **7**, 6663–6674.
23 A. J. Hoffman, J. S. Bates, J. R. D. Iorio, S. V. Nystrom, C. T. Nimlos, R. Gounder and D. Hibbitts, *Angew. Chem., Int. Ed.*, 2020, **59**, 18686–18694.
24 J. S. Bates, B. C. Bukowski, J. Greeley and R. Gounder, *Chem. Sci.*, 2020, **11**, 7102–7122.
25 Y. Shen, T. T. Le, D. Fu, J. E. Schmidt, M. Filez, B. M. Weckhuysen and J. D. Rimer, *ACS Catal.*, 2018, **8**, 11042–11053.
26 Z. S. B. Sousa, D. V. Cesar, C. A. Henriques and V. T. Da Silva, *Catal. Today*, 2014, **234**, 182–191.
27 Z. Shi and A. Bhan, *J. Catal.*, 2023, **421**, 198–209.
28 J. H. Ahn, R. Kolvenbach, S. S. Al-Khattaf, A. Jentys and J. A. Lercher, *ACS Catal.*, 2013, **3**, 817–825.
29 J. H. Ahn, R. Kolvenbach, O. Y. Gutiérrez, S. S. Al-Khattaf, A. Jentys and J. A. Lercher, *Microporous Mesoporous Mater.*, 2015, **210**, 52–59.
30 D. Parmar, S. H. Cha, T. Salavati-fard, A. Agarwal, H. Chiang, S. M. Washburn, J. C. Palmer, L. C. Grabow and J. D. Rimer, *J. Am. Chem. Soc.*, 2022, **144**, 7861–7870.
31 D. Parmar, S. H. Cha, C. Huang, H. Chiang, S. Washburn, L. C. Grabow and J. D. Rimer, *Catal. Sci. Technol.*, 2023, **13**, 5227–5236.
32 S. Wang and E. Iglesia, *J. Catal.*, 2017, **352**, 415–435.
33 E. S. Vasiliadou, N. S. Gould and R. F. Lobo, *ChemCatChem*, 2017, **9**, 4417–4425.
34 P. B. Weisz, *Pure Appl. Chem.*, 1980, **52**, 2091–2103.
35 S. M. Csicsery, *Zeolites*, 1984, **4**, 202–213.
36 J. Weitkamp, S. Ernst and L. Puppe, in *Catalysis and Zeolites: Fundamentals and Applications*, ed. J. Weitkamp and L. Puppe, Springer, Berlin, Heidelberg, 1999, pp. 327–376.
37 T. F. Degnan, *J. Catal.*, 2003, **216**, 32–46.
38 A. Bhan and E. Iglesia, *Acc. Chem. Res.*, 2008, **41**, 559–567.
39 R. Gounder and E. Iglesia, *Chem. Commun.*, 2013, **49**, 3491–3509.
40 E. G. Derouane, *J. Catal.*, 1986, **100**, 541–544.
41 F. Eder and J. A. Lercher, *J. Phys. Chem. B*, 1997, **101**, 1273–1278.
42 S. Wang, I. Agirrezabal-Telleria, A. Bhan, D. Simonetti, K. Takanabe and E. Iglesia, *Faraday Discuss.*, 2017, **197**, 9–39.
43 M. L. Sarazen and E. Iglesia, *ChemCatChem*, 2018, **10**, 4028–4037.
44 E. Iglesia, *Catalysis in Chemistry and Biology*, World Scientific, 2018, pp. 148–155.
45 P. Deshlahra and E. Iglesia, *Chem. Commun.*, 2020, **56**, 7371–7398.
46 B. C. Knott, C. T. Nimlos, D. J. Robichaud, M. R. Nimlos, S. Kim and R. Gounder, *ACS Catal.*, 2018, **8**, 770–784.
47 E. E. Bickel, C. T. Nimlos and R. Gounder, *J. Catal.*, 2021, **399**, 75–85.
48 B. E. R. Snyder, P. Vanelderen, M. L. Bols, S. D. Hallaert, L. H. Böttger, L. Ungur, K. Pierloot, R. A. Schoonheydt, B. F. Sels and E. I. Solomon, *Nature*, 2016, **536**, 317–321.
49 D. K. Pappas, E. Borfecchia, M. Dyballa, I. A. Pankin, K. A. Lomachenko, A. Martini, M. Signorile, S. Teketel, B. Arstad, G. Berlier, C. Lamberti, S. Bordiga, U. Olsbye, K. P. Lillerud, S. Svelle and P. Beato, *J. Am. Chem. Soc.*, 2017, **139**, 14961–14975.
50 D. T. Bregante, L. N. Wilcox, C. Liu, C. Paolucci, R. Gounder and D. W. Flaherty, *ACS Catal.*, 2021, **11**, 11873–11884.
51 R. W. Borry, Y. H. Kim, A. Huffsmith, J. A. Reimer and E. Iglesia, *J. Phys. Chem. B*, 1999, **103**, 5787–5796.
52 W. Ding, G. D. Meitzner and E. Iglesia, *J. Catal.*, 2002, **206**, 14–22.
53 Á. N. Santiago-Colón and R. Gounder, *J. Catal.*, 2024, **430**, 115335.
54 J. A. Biscardi and E. Iglesia, *Catal. Today*, 1996, **31**, 207–231.
55 N. M. Phadke, J. Van der Mynsbrugge, E. Mansoor, A. B. Getsoian, M. Head-Gordon and A. T. Bell, *ACS Catal.*, 2018, **8**, 6106–6126.
56 Y. Yuan, R. F. Lobo and B. Xu, *ACS Catal.*, 2022, 1775–1783.
57 A. Finiels, F. Fajula and V. Hulea, *Catal. Sci. Technol.*, 2014, **4**, 2412–2426.
58 R. Joshi, G. Zhang, J. T. Miller and R. Gounder, *ACS Catal.*, 2018, **8**, 11407–11422.
59 E. Borfecchia, P. Beato, S. Svelle, U. Olsbye, C. Lamberti and S. Bordiga, *Chem. Soc. Rev.*, 2018, **47**, 8097–8133.
60 C. Paolucci, J. R. Di Iorio, W. F. Schneider and R. Gounder, *Acc. Chem. Res.*, 2020, **53**, 1881–1892.
61 V. Valtchev, G. Majano, S. Mintova and J. Pérez-Ramírez, *Chem. Soc. Rev.*, 2013, **42**, 263–290.
62 V. Valtchev and L. Tosheva, *Chem. Rev.*, 2013, **113**, 6734–6760.
63 W. J. Roth, P. Nachtigall, R. E. Morris and J. Čejka, *Chem. Rev.*, 2014, **114**, 4807–4837.
64 J. D. Rimer, M. Kumar, R. Li, A. I. Lupulescu and M. D. Oleksiak, *Catal. Sci. Technol.*, 2014, **4**, 3762–3771.
65 Z. Qin, J.-P. Gilson and V. Valtchev, *Curr. Opin. Chem. Eng.*, 2015, **8**, 1–6.
66 K. N. Olafson, R. Li, B. G. Alamani and J. D. Rimer, *Chem. Mater.*, 2016, **28**, 8453–8465.
67 N. Masoumifard, R. Guillet-Nicolas and F. Kleitz, *Adv. Mater.*, 2018, **30**, 1704439.
68 J. Přech, P. Pizarro, D. P. Serrano and J. Čejka, *Chem. Soc. Rev.*, 2018, **47**, 8263–8306.
69 J. D. Rimer, A. Chawla and T. T. Le, *Annu. Rev. Chem. Biomol. Eng.*, 2018, **9**, 283–309.
70 R. Bai, Y. Song, Y. Li and J. Yu, *Trends Chem.*, 2019, **1**, 601–611.
71 S. Li, J. Li, M. Dong, S. Fan, T. Zhao, J. Wang and W. Fan, *Chem. Soc. Rev.*, 2019, **48**, 885–907.
72 D. Zhang, C. Jin, M. Zou and S. Huang, *Chem. – Eur. J.*, 2019, **25**, 2675–2683.
73 L.-H. Chen, M.-H. Sun, Z. Wang, W. Yang, Z. Xie and B.-L. Su, *Chem. Rev.*, 2020, **120**, 11194–11294.
74 S. Li, H. Yang, S. Wang, J. Wang, W. Fan and M. Dong, *Chem. Commun.*, 2022, **58**, 2041–2054.
75 A. J. Mallette, S. Seo and J. D. Rimer, *Nat. Synth.*, 2022, **1**, 521–534.
76 I. C. Medeiros-Costa, E. Dib, N. Nesterenko, J.-P. Dath, J.-P. Gilson and S. Mintova, *Chem. Soc. Rev.*, 2021, **50**, 11156–11179.
77 G. Noh and M. L. Sarazen, *J. Catal.*, 2021, **404**, 679–686.
78 S. Lee, Y. Park and M. Choi, *ACS Catal.*, 2024, 2031–2048.
79 J. Dědeček, Z. Sobalík and B. Wichterlová, *Catal. Rev.*, 2012, **54**, 135–223.

Open Access Article. Published on 20 September 2024. Downloaded on 1/24/2026 9:35:52 AM. This article is licensed under a Creative Commons Attribution-NonCommercial 3.0 Unported Licence.

80 J. Dědeček, E. Tabor and S. Sklenak, *ChemSusChem*, 2019, **12**, 556–576.
81 M. Shamzhy, M. Opanasenko, P. Concepción and A. Martínez, *Chem. Soc. Rev.*, 2019, **48**, 1095–1149.
82 S. Wang, Y. He, W. Jiao, J. Wang and W. Fan, *Curr. Opin. Chem. Eng.*, 2019, **23**, 146–154.
83 A. Palčić and V. Valtchev, *Appl. Catal., A.*, 2020, **606**, 117795.
84 T. T. Le, A. Chawla and J. D. Rimer, *J. Catal.*, 2020, **391**, 56–68.
85 S. J. Kwak, H. S. Kim, N. Park, M.-J. Park and W. B. Lee, *Korean J. Chem. Eng.*, 2021, **38**, 1117–1128.
86 J. Li, M. Gao, W. Yan and J. Yu, *Chem. Sci.*, 2023, **14**, 1935–1959.
87 J. Bae and M. Dusselier, *Chem. Commun.*, 2023, **59**, 852–867.
88 R. F. Lobo, in *Handbook of Zeolite Science and Technology*, ed. S. Auerbach, K. Carrado and P. Dutta, Marcel Dekker, Inc., New York, Basel, 2003, pp. 80–112.
89 C. Baerlocher and L. B. McCusker, Database of Zeolite Structures, **https://www.iza-structure.org/databases/**, (accessed April 18, 2024).
90 M. D. Foster, I. Rivin, M. M. J. Treacy and O. Delgado Friedrichs, *Microporous Mesoporous Mater.*, 2006, **90**, 32–38.
91 E. Haldoupis, S. Nair and D. S. Sholl, *Phys. Chem. Chem. Phys.*, 2011, **13**, 5053–5060.
92 E. L. First, C. E. Gounaris, J. Wei and C. A. Floudas, *Phys. Chem. Chem. Phys.*, 2011, **13**, 17339–17358.
93 T. F. Willems, C. H. Rycroft, M. Kazi, J. C. Meza and M. Haranczyk, *Microporous Mesoporous Mater.*, 2012, **149**, 134–141.
94 A. J. Jones, C. Ostrouchov, M. Haranczyk and E. Iglesia, *Microporous Mesoporous Mater.*, 2013, **181**, 208–216.
95 M. Pinheiro, R. L. Martin, C. H. Rycroft, A. Jones, E. Iglesia and M. Haranczyk, *J. Mol. Graphics. Modell.*, 2013, **44**, 208–219.
96 M. Pinheiro, R. L. Martin, C. H. Rycroft and M. Haranczyk, *CrystEngComm*, 2013, **15**, 7531–7538.
97 J. T. Crum, J. R. Crum, C. Taylor and W. F. Schneider, *Microporous Mesoporous Mater.*, 2023, **351**, 112466.
98 C. E. Webster, R. S. Drago and M. C. Zerner, *J. Phys. Chem. B*, 1999, **103**, 1242–1249.
99 C. D. Chang and A. T. Bell, *Catal. Lett.*, 1991, **8**, 305–316.
100 S. L. Burkett and M. E. Davis, *J. Phys. Chem.*, 1994, **98**, 4647–4653.
101 S. L. Burkett and M. E. Davis, *Chem. Mater.*, 1995, **7**, 920–928.
102 S. L. Burkett and M. E. Davis, *Chem. Mater.*, 1995, **7**, 1453–1463.
103 C. S. Cundy and P. A. Cox, *Microporous Mesoporous Mater.*, 2005, **82**, 1–78.
104 M. D. Oleksiak, J. A. Soltis, M. T. Conato, R. L. Penn and J. D. Rimer, *Chem. Mater.*, 2016, **28**, 4906–4916.
105 M. Kumar, M. K. Choudhary and J. D. Rimer, *Nat. Commun.*, 2018, **9**, 1–9.
106 D. Parmar, Z. Niu, Y. Liang, H. Dai and J. D. Rimer, *Faraday Discuss.*, 2022, **235**, 322–342.
107 A. J. Mallette, K. Shilpa and J. D. Rimer, *Chem. Rev.*, 2024, **124**, 3416–3493.
108 H. Gies and B. Marler, *Zeolites*, 1992, **12**, 42–49.
109 D. F. Shantz and R. F. Lobo, *Chem. Mater.*, 1998, **10**, 4015–4024.
110 D. F. Shantz and R. F. Lobo, *J. Am. Chem. Soc.*, 1998, **120**, 2482–2483.
111 D. F. Shantz, J. Schmedt auf der Günne, H. Koller and R. F. Lobo, *J. Am. Chem. Soc.*, 2000, **122**, 6659–6663.
112 M. B. Park, D. Jo, H. C. Jeon, C. P. Nicholas, G. J. Lewis and S. B. Hong, *Chem. Mater.*, 2014, 11.
113 D. F. Shantz, C. Fild, H. Koller and R. F. Lobo, *J. Phys. Chem. B*, 1999, **103**, 10858–10865.
114 D. F. Shantz, R. F. Lobo, C. Fild and H. Koller, in *Studies in Surface Science and Catalysis*, ed. A. Corma, F. V. Melo, S. Mendioroz and J. L. G. Fierro, Elsevier, 2000, vol. 130, pp. 845–850.
115 M. J. Sabater and G. Sastre, *Chem. Mater.*, 2001, **13**, 4520–4526.
116 G. Sastre, V. Fornes and A. Corma, *J. Phys. Chem. B*, 2002, **106**, 701–708.
117 A. B. Pinar, C. Márquez-Álvarez, M. Grande-Casas and J. Pérez-Pariente, *J. Catal.*, 2009, **263**, 258–265.
118 Y. Román-Leshkov, M. Moliner and M. E. Davis, *J. Phys. Chem. C*, 2011, **115**, 1096–1102.
119 A. B. Pinar, L. Gómez-Hortigüela, L. B. McCusker and J. Pérez-Pariente, *Chem. Mater.*, 2013, **25**, 3654–3661.
120 A. B. Pinar, P. A. Wright, L. Gómez-Hortigüela and J. Pérez-Pariente, *Microporous Mesoporous Mater.*, 2010, **129**, 164–172.
121 L. Gómez-Hortigüela, A. B. Pinar, F. Corà and J. Pérez-Pariente, *Chem. Commun.*, 2010, **46**, 2073–2075.
122 A. B. Pinar, L. Gomez-Hortiguela and J. Perez-Pariente, *Chem. Mater.*, 2007, **19**, 5617–5626.
123 A. B. Pinar, R. García, L. Gómez-Hortigüela and J. Pérez-Pariente, *Top. Catal.*, 2010, **53**, 1297–1303.
124 W. Chu, X. Liu, Z. Yang, H. Nakata, X. Tan, X. Liu, L. Xu, P. Guo, X. Li and X. Zhu, *Chin. J. Catal.*, 2021, **42**, 2078–2087.
125 Y. Guo, S. Wang, R. Geng, P. Wang, S. Li, M. Dong, Z. Qin, J. Wang and W. Fan, *iScience*, 2023, **26**, 107748.
126 A. B. Pinar, P. Rzepka, A. J. Knorpp, L. B. McCusker, C. Baerlocher, T. Huthwelker and J. A. van Bokhoven, *J. Am. Chem. Soc.*, 2021, **143**, 17926–17930.
127 G. T. Kokotailo, S. L. Lawton, D. H. Olson and W. M. Meier, *Nature*, 1978, **272**, 437–438.
128 D. H. Olson, G. T. Kokotailo, S. L. Lawton and W. M. Meier, *J. Phys. Chem.*, 1981, **85**, 2238–2243.
129 H. van Koningsveld, *Acta Crystallogr., Sect. B: Struct. Sci.*, 1990, **46**, 731–735.
130 C. T. Nimlos, A. J. Hoffman, Y. G. Hur, B. J. Lee, J. R. Di Iorio, D. D. Hibbitts and R. Gounder, *Chem. Mater.*, 2020, **32**, 9277–9298.
131 S. Ezenwa, H. Montalvo-Castro, A. J. Hoffman, H. Locht, J. Attebery, D.-Y. Jan, M. Schmithorst, B. Chmelka, D. Hibbitts and R. Gounder, *J. Am. Chem. Soc.*, 2024, **146**, 10666–10678.
132 R. J. Argauer and G. R. Landolt, *US Pat.*, US3702886A, 1972.
133 X. Tang, W. Chen, W. Dong, Z. Liu, J. Yuan, H. Xia, X. Yi and A. Zheng, *Catal. Today*, 2022, **405–406**, 101–110.
134 E. Dib, T. Mineva, E. Veron, V. Sarou-Kanian, F. Fayon and B. Alonso, *J. Phys. Chem. Lett.*, 2018, **9**, 19–24.
135 T. Yokoi, H. Mochizuki, S. Namba, J. N. Kondo and T. Tatsumi, *J. Phys. Chem. C*, 2015, **119**, 15303–15315.
136 T. Yokoi, H. Mochizuki, T. Biligetu, Y. Wang and T. Tatsumi, *Chem. Lett.*, 2017, **46**, 798–800.
137 T. Biligetu, Y. Wang, T. Nishitoba, R. Otomo, S. Park, H. Mochizuki, J. N. Kondo, T. Tatsumi and T. Yokoi, *J. Catal.*, 2017, **353**, 1–10.
138 S. Park, T. Biligetu, Y. Wang, T. Nishitoba, J. N. Kondo and T. Yokoi, *Catal. Today*, 2018, **303**, 64–70.
139 B. M. Lok, T. R. Cannan and C. A. Messina, *Zeolites*, 1983, **3**, 282–291.
140 Z. Gabelica, M. Cavez-Bierman, P. Bodart, A. Gourgue and J. B. Nagy, in *Studies in Surface Science and Catalysis*, ed. B. Držaj, S. Hočevar and S. Pejovnik, Elsevier, 1985, vol. 24, pp. 55–63.
141 E. W. Valyocsik and L. D. Rollmann, *Zeolites*, 1985, **5**, 123–125.
142 F. J. Van Der Gaag, J. C. Jansen and H. Van Bekkum, *Appl. Catal.*, 1985, **17**, 261–271.
143 A. Araya and B. M. Lowe, *Zeolites*, 1986, **6**, 111–118.
144 In *Studies in Surface Science and Catalysis*, ed. P. A. Jacobs and J. A. Martens, Elsevier, 1987, vol. 33, pp. 147–166.
145 S. Schwarz, M. Kojima and C. T. O'Connor, *Appl. Catal.*, 1991, **73**, 313–330.
146 L. D. Rollmann, J. L. Schlenker, S. L. Lawton, C. L. Kennedy, G. J. Kennedy and D. J. Doren, *J. Phys. Chem. B*, 1999, **103**, 7175–7183.
147 L. D. Rollmann, J. L. Schlenker, C. L. Kennedy, G. J. Kennedy and D. J. Doren, *J. Phys. Chem. B*, 2000, **104**, 721–726.
148 S. Zanardi, A. Alberti, R. Millini, G. Bellussi and G. Perego, in *Studies in Surface Science and Catalysis*, ed. R. Aiello, G. Giordano and F. Testa, Elsevier, 2002, vol. 142, pp. 1923–1930.
149 G. Perego, G. Bellussi, R. Millini, A. Alberti and S. Zanardi, *Microporous Mesoporous Mater.*, 2003, **58**, 213–223.
150 S. Sang, F. Chang, Z. Liu, C. He, Y. He and L. Xu, *Catal. Today*, 2004, **93–95**, 729–734.
151 H. Lee, S. I. Zones and M. E. Davis, *J. Phys. Chem. B*, 2005, **109**, 2187–2191.
152 H. Yu, X. Wang and Y. Long, *Microporous Mesoporous Mater.*, 2006, **95**, 234–240.
153 H. Wang, P. L. Bogdan and R. R. Willis, *US Pat.*, US20110282122A1, 2011.
154 S. H. Keoh, W. Chaikittisilp, K. Muraoka, R. R. Mukti, A. Shimojima, P. Kumar, M. Tsapatsis and T. Okubo, *Chem. Mater.*, 2016, **28**, 8997–9007.
155 L. Meng, B. Mezari, M. G. Goesten and E. J. M. Hensen, *Chem. Mater.*, 2017, **29**, 4091–4096.

 This journal is © The Royal Society of Chemistry 2024

Open Access Article. Published on 20 September 2024. Downloaded on 1/24/2026 9:35:52 AM. This article is licensed under a Creative Commons Attribution-NonCommercial 3.0 Unported Licence.

156 D. Fu, J. E. Schmidt, Z. Ristanović, A. D. Chowdhury, F. Meirer and B. M. Weckhuysen, *Angew. Chem., Int. Ed.*, 2017, **56**, 11217–11221.
157 D. Jo and S. B. Hong, *Chem. Commun.*, 2018, **54**, 487–490.
158 H. Liu, H. Wang, A.-H. Xing and J.-H. Cheng, *J. Phys. Chem. C*, 2019, **123**, 15637–15647.
159 J. Ma, K. Hidaka, M. Ogura and T. Moteki, *Cryst. Growth Des.*, 2023, **23**, 8499–8508.
160 S. Ren, F. Yang, C. Tian, Y. Yue, W. Zou, W. Hua and Z. Gao, *Catalysts*, 2023, **13**, 1295.
161 Y. Wang, X. He, F. Yang, Z. Su and X. Zhu, *Ind. Eng. Chem. Res.*, 2020, **59**, 13420–13427.
162 L. Guan, M. Liu, H. Liu, L. Zhang, Y. Zhang, Y. Qin, B. He, Y. Mei and Y. Zu, *Fuel*, 2023, **353**, 129230.
163 L. Zhao, P.-P. Xiao, Y. Wang, Y. Lu, T. M. Karim, H. Gies and T. Yokoi, *ACS Appl. Mater. Interfaces*, 2024, **16**(14), 17701–17714.
164 R. Gounder, C. T. Nimlos and B. J. Lee, *US Pat.*, US11851337B2, 2023.
165 J. T. Miller, R. Gounder, F. H. Ribeiro, H.-T. Tseng, P. M. Kester, Y. G. Hur and Y. R. Cho, *US Pat.*, US11358912B2, 2022.
166 K. Morgan, G. Gainsford and N. Milestone, *J. Chem. Soc., Chem. Commun.*, 1995, 425–426.
167 Y. Wang, J. Yu, Y. Li, Z. Shi and R. Xu, *Chem. – Eur. J.*, 2003, **9**, 5048–5055.
168 L. Gómez-Hortigüela, T. Álvaro-Muñoz, B. Bernardo-Maestro and J. Pérez-Pariente, *Phys. Chem. Chem. Phys.*, 2014, **17**, 348–357.
169 B. Bernardo-Maestro, F. López-Arbeloa, J. Pérez-Pariente and L. Gómez-Hortigüela, *J. Phys. Chem. C*, 2015, **119**, 28214–28225.
170 L. Gómez-Hortigüela and B. Bernardo-Maestro, in *Insights into the Chemistry of Organic Structure-Directing Agents in the Synthesis of Zeolitic Materials*, ed. L. Gómez-Hortigüela, Springer International Publishing, Cham, 2017, vol. 175, pp. 201–244.
171 L. Gómez-Hortigüela and M. Á. Camblor, in *Insights into the Chemistry of Organic Structure-Directing Agents in the Synthesis of Zeolitic Materials*, ed. L. Gómez-Hortigüela, Springer International Publishing, Cham, 2018, pp. 1–41.
172 B. Bernardo-Maestro, J. Li, J. Pérez-Pariente, F. López-Arbeloa and L. Gómez-Hortigüela, *Chem. – Eur. J.*, 2022, **28**, e202200702.
173 H. Jongkind, K. P. Datema, S. Nabuurs, A. Seive and W. H. J. Stork, *Microporous Mater.*, 1997, **10**, 149–161.
174 M. Wang, S. Huang, J. Lü, Z. Cheng, Y. Li, S. Wang and X. Ma, *Chin. J. Catal.*, 2016, **37**, 1530–1537.
175 Y. Li, M. Yu, K. Cai, M. Wang, J. Lv, R. F. Howe, S. Huang and X. Ma, *Phys. Chem. Chem. Phys.*, 2020, **22**, 11374–11381.
176 F. Chen, X.-B. Feng, L.-Y. Zhang, J.-P. Zhao, Z.-M. He, F.-J. Yi, X.-Y. Zhao and J.-P. Cao, *Chem. Eng. Sci.*, 2022, **263**, 118110.
177 L. Wang, H. Pan, J. Qian, K. Yan, X. Yang, L. Liu, G. Song and H. Zhu, *Microporous Mesoporous Mater.*, 2023, **354**, 112569.
178 M. Liu, T. Yokoi, M. Yoshioka, H. Imai, J. N. Kondo and T. Tatsumi, *Phys. Chem. Chem. Phys.*, 2014, **16**, 4155–4164.
179 Z. Wang, W. Chu, Z. Zhao, Z. Liu, H. Chen, D. Xiao, K. Gong, F. Li, X. Li and G. Hou, *J. Phys. Chem. Lett.*, 2021, **12**, 9398–9406.
180 Z. J. Berkson, M.-F. Hsieh, S. Smeets, D. Gajan, A. Lund, A. Lesage, D. Xie, S. I. Zones, L. B. McCusker, C. Baerlocher and B. F. Chmelka, *Angew. Chem., Int. Ed.*, 2019, **58**, 6255–6259.
181 K. Muraoka, W. Chaikittisilp, Y. Yanaba, T. Yoshikawa and T. Okubo, *Angew. Chem., Int. Ed.*, 2018, **57**, 3742–3746.
182 J. Datka, B. Gil and A. Kubacka, *Zeolites*, 1997, **18**, 245–249.
183 M. A. Makarova, A. E. Wilson, B. J. van Liemt, C. M. A. M. Mesters, A. W. de Winter and C. Williams, *J. Catal.*, 1997, **172**, 170–177.
184 V. A. Veefkind, M. L. Smidt and J. A. Lercher, *Appl. Catal., A*, 2000, **194–195**, 319–332.
185 A. Bhan, A. D. Allian, G. J. Sunley, D. J. Law and E. Iglesia, *J. Am. Chem. Soc.*, 2007, **129**, 4919–4924.
186 M. Maache, A. Janin, J. C. Lavalley and E. Benazzi, *Zeolites*, 1995, **15**, 507–516.
187 N. S. Nesterenko, F. Thibault-Starzyk, V. Montouillout, V. V. Yuschenko, C. Fernandez, J.-P. Gilson, F. Fajula and I. I. Ivanova, *Microporous Mesoporous Mater.*, 2004, **71**, 157–166.
188 S. Liu, H. Liu, X. Ma, Y. Liu, W. Zhu and Z. Liu, *Catal. Sci. Technol.*, 2020, **10**, 4663–4672.
189 R. Liu, S. Zeng, T. Sun, S. Xu, Z. Yu, Y. Wei and Z. Liu, *ACS Catal.*, 2022, 4491–4500.
190 J. R. Carpenter, S. Yeh, S. I. Zones and M. E. Davis, *J. Catal.*, 2010, **269**, 64–70.
191 S. I. Zones and T. V. Harris, *Microporous Mesoporous Mater.*, 2000, **35–36**, 31–46.
192 E. Besset, D. Meloni, D. Martin, M. Guisnet and L. Schreyeck, in *Studies in Surface Science and Catalysis*, ed. B. Delmon and G. F. Froment, Elsevier, 1999, vol. 126, pp. 171–178.
193 D. Meloni, D. Martin and M. Guisnet, *Appl. Catal., A*, 2001, **215**, 67–79.
194 P. Matias, J. M. Lopes, S. Laforge, P. Magnoux, M. Guisnet and F. Ramôa Ribeiro, *Appl. Catal., A*, 2008, **351**, 174–183.
195 S. Laforge, D. Martin, J. L. Paillaud and M. Guisnet, *J. Catal.*, 2003, **220**, 92–103.
196 S. Laforge, D. Martin and M. Guisnet, *Microporous Mesoporous Mater.*, 2004, **67**, 235–244.
197 J. Chen, T. Liang, J. Li, S. Wang, Z. Qin, P. Wang, L. Huang, W. Fan and J. Wang, *ACS Catal.*, 2016, **6**, 2299–2313.
198 T. Liang, J. Chen, S. Wang, P. Wang, Z. Qin, F. Jin, M. Dong, J. Wang and W. Fan, *Catal. Sci. Technol.*, 2022, **12**, 6268–6284.
199 Y. Ding, D. Miao, Z. Wang, J. Feng, P. Zhang, R. Yu, X. Cao, X. Pan and X. Bao, *ACS Catal.*, 2023, **13**, 14277–14284.
200 P. M. Kester, J. T. Miller and R. Gounder, *Ind. Eng. Chem. Res.*, 2018, **57**, 6673–6683.
201 C. T.-W. Chu, G. H. Kuehl, R. M. Lago and C. D. Chang, *J. Catal.*, 1985, **93**, 451–458.
202 Q. Zhu, J. N. Kondo, T. Yokoi, T. Setoyama, M. Yamaguchi, T. Takewaki, K. Domen and T. Tatsumi, *Phys. Chem. Chem. Phys.*, 2011, **13**, 14598–14605.
203 A. J. Jones, R. T. Carr, S. I. Zones and E. Iglesia, *J. Catal.*, 2014, **312**, 58–68.
204 S. I. Zones, L. T. Yuen, Y. Nakagawa, R. A. Van NORDSTRAND and S. D. Toto, in *Proceedings from the Ninth International Zeolite Conference*, ed. R. von Ballmoos, J. B. Higgins and M. M. J. Treacy, Butterworth-Heinemann, 1993, pp. 163–170.
205 C. Y. Chen and S. I. Zones, in *Studies in Surface Science and Catalysis*, ed. A. Galarneau, F. Fajula, F. Di Renzo and J. Vedrine, Elsevier, 2001, vol. 135, p. 211.
206 H. Koller, C.-Y. Chen and S. I. Zones, *Top. Catal.*, 2015, **58**, 451–479.
207 S. I. Zones, A. Benin, S.-J. Hwang, D. Xie, S. Elomari and M.-F. Hsieh, *J. Am. Chem. Soc.*, 2014, **136**, 1462–1471.
208 C. Schroeder, C. M. Lew, S. I. Zones and H. Koller, *Chem. Mater.*, 2022, **34**, 3479–3488.
209 S. I. Zones, C. Y. Chen, A. Benin and S.-J. Hwang, *J. Catal.*, 2013, **308**, 213–225.
210 S. I. Zones, C. Y. Chen, A. Corma, M. T. Cheng, C. L. Kibby, I. Y. Chan and A. W. Burton, *J. Catal.*, 2007, **250**, 41–54.
211 S. I. Zones, J. Ruan, S. Elomari, O. Terasaki, C. Y. Chen and A. Corma, *Solid State Sci.*, 2011, **13**, 706–713.
212 J. C. Vega-Vila, J. W. Harris and R. Gounder, *J. Catal.*, 2016, **344**, 108–120.
213 G. L. Woolery, G. H. Kuehl, H. C. Timken, A. W. Chester and J. C. Vartuli, *Zeolites*, 1997, **19**, 288–296.
214 E. Lippmaa, A. Samoson and M. Magi, *J. Am. Chem. Soc.*, 1986, **108**, 1730–1735.
215 O. H. Han, C.-S. Kim and S. B. Hong, *Angew. Chem., Int. Ed.*, 2002, **41**, 469–472.
216 S. Sklenak, J. Dědeček, C. Li, B. Wichterlová, V. Gábová, M. Sierka and J. Sauer, *Angew. Chem., Int. Ed.*, 2007, **46**, 7286–7289.
217 J. Dědeček, S. Sklenak, C. Li, B. Wichterlová, V. Gábová, J. Brus, M. Sierka and J. Sauer, in *Studies in Surface Science and Catalysis*, ed. A. Gédéon, P. Massiani and F. Babonneau, Elsevier, 2008, vol. 174, pp. 781–786.
218 S. Sklenak, J. Dědeček, C. Li, B. Wichterlová, V. Gábová, M. Sierka and J. Sauer, *Phys. Chem. Chem. Phys.*, 2009, **11**, 1237–1247.
219 J. Holzinger, P. Beato, L. F. Lundegaard and J. Skibsted, *J. Phys. Chem. C*, 2018, **122**, 15595–15613.
220 S. Al-Nahari, E. Dib, C. Cammarano, E. Saint-Germes, D. Massiot, V. Sarou-Kanian and B. Alonso, *Angew. Chem., Int. Ed.*, 2023, **62**, e202217992.
221 Y. Zhou, Y. Mu, M.-F. Hsieh, B. Kabius, C. Pacheco, C. Bator, R. M. Rioux and J. D. Rimer, *J. Am. Chem. Soc.*, 2020, **142**, 8211–8222.
222 A. Abraham, S.-H. Lee, C.-H. Shin, S. B. Hong, R. Prins and J. A. van Bokhoven, *Phys. Chem. Chem. Phys.*, 2004, **6**, 3031–3036.

Open Access Article. Published on 20 September 2024. Downloaded on 1/24/2026 9:35:52 AM. This article is licensed under a Creative Commons Attribution-NonCommercial 3.0 Unported Licence.

223 A. Vjunov, J. L. Fulton, T. Huthwelker, S. Pin, D. Mei, G. K. Schenter, N. Govind, D. M. Camaioni, J. Z. Hu and J. A. Lercher, *J. Am. Chem. Soc.*, 2014, **136**, 8296–8306.
224 A. Vjunov, J. L. Fulton, T. Huthwelker, S. Pin, D. Mei, G. K. Schenter, N. Govind, D. M. Camaioni, J. Z. Hu and J. A. Lercher, *J. Am. Chem. Soc.*, 2015, **137**, 2409.
225 R. Otomo, T. Nishitoba, R. Osuga, Y. Kunitake, Y. Kamiya, T. Tatsumi and T. Yokoi, *J. Phys. Chem. C*, 2018, **122**, 1180–1191.
226 K. Chen, S. Horstmeier, Vy. T. Nguyen, B. Wang, S. P. Crossley, T. Pham, Z. Gan, I. Hung and J. L. White, *J. Am. Chem. Soc.*, 2020, **142**, 7514–7523.
227 K. Chen, Z. Gan, S. Horstmeier and J. L. White, *J. Am. Chem. Soc.*, 2021, **143**, 6669–6680.
228 A. B. Pinar, R. Verel, J. Pérez-Pariente and J. A. van Bokhoven, *Microporous Mesoporous Mater.*, 2014, **193**, 111–114.
229 J. Dedecek, M. J. Lucero, C. Li, F. Gao, P. Klein, M. Urbanova, Z. Tvaruzkova, P. Sazama and S. Sklenak, *J. Phys. Chem. C*, 2011, **115**, 11056–11064.
230 S. Smeets, L. B. McCusker, C. Baerlocher, S. Elomari, D. Xie and S. I. Zones, *J. Am. Chem. Soc.*, 2016, **138**, 7099–7106.
231 H. M. Rietveld, *J. Appl. Crystallogr.*, 1969, **2**, 65–71.
232 S. Smeets, L. B. McCusker, C. Baerlocher, D. Xie, C.-Y. Chen and S. I. Zones, *J. Am. Chem. Soc.*, 2015, **137**, 2015–2020.
233 Y. Ma, L. Wang, L. Chen, M. Shen, X. Yang, T. Wang, F. Yuan, Y. Zhou, J. Wang and H. Zhu, *CrystEngComm*, 2022, **24**, 2118–2125.
234 W. I. F. David and K. Shankland, *Acta Crystallogr., Sect. A: Found. Crystallogr.*, 2008, **64**, 52–64.
235 R. Bohinc, J. Hoszowska, J.-C. Dousse, W. Błachucki, F. Zeeshan, Y. Kayser, M. Nachtegaal, A. B. Pinar and J. A. van Bokhoven, *Phys. Chem. Chem. Phys.*, 2017, **19**, 29271–29277.
236 J. A. van Bokhoven, T.-L. Lee, M. Drakopoulos, C. Lamberti, S. Thieß and J. Zegenhagen, *Nat. Mater.*, 2008, **7**, 551–555.
237 K. Hadjiivanov, in *Advances in Catalysis*, ed. F. C. Jentoft, Academic Press, 2014, vol. 57, pp. 99–318.
238 C. A. Emeis, *J. Catal.*, 1993, **141**, 347–354.
239 M. A. Makarova, V. L. Zholobenko, K. M. Al-Ghefaili, N. E. Thompson, J. Dewing and J. Dwyer, *J. Chem. Soc., Faraday Trans.*, 1994, **90**, 1047–1054.
240 V. L. Zholobenko, D. B. Lukyanov, J. Dwyer and W. J. Smith, *J. Phys. Chem. B*, 1998, **102**, 2715–2721.
241 P. A. Jacobs and W. J. Mortier, *Zeolites*, 1982, **2**, 226–230.
242 T. Bucko, L. Benco, T. Demuth and J. Hafner, *J. Chem. Phys.*, 2002, **117**, 7295–7305.
243 J. A. Lercher and A. Jentys, in *Studies in Surface Science and Catalysis*, ed. J. Čejka, H. van Bekkum, A. Corma and F. Schüth, Elsevier, 2007, vol. 168, pp. 435–476.
244 S. Bordiga, C. Lamberti, F. Bonino, A. Travert and F. Thibault-Starzyk, *Chem. Soc. Rev.*, 2015, **44**, 7262–7341.
245 L. Lakiss, A. Vicente, J.-P. Gilson, V. Valtchev, S. Mintova, A. Vimont, R. Bedard, S. Abdo and J. Bricker, *ChemPhysChem*, 2020, **21**, 1873–1881.
246 A. A. Gabrienko, I. G. Danilova, S. S. Arzumanov, L. V. Pirutko, D. Freude and A. G. Stepanov, *J. Phys. Chem. C*, 2018, **122**, 25386–25395.
247 P. A. Jacobs and R. Von Ballmoos, *J. Phys. Chem.*, 1982, **86**, 3050–3052.
248 T. R. Hughes and H. M. White, *J. Phys. Chem.*, 1967, **71**, 2192–2201.
249 B. Athokpam, S. G. Ramesh and R. H. McKenzie, *Chem. Phys.*, 2017, **488–489**, 43–54.
250 H. Tsubomura, *J. Chem. Phys.*, 1956, **24**, 927–931.
251 L. Treps, C. Demaret, D. Wisser, B. Harbuzaru, A. Méthivier, E. Guillon, D. V. Benedis, A. Gomez, T. D. Bruin, M. Rivallan, L. Catita, A. Lesage and C. Chizallet, *J. Phys. Chem. C*, 2021, **125**, 2163–2181.
252 R. A. Schoonheydt and J. B. Uytterhoeven, *J. Catal.*, 1970, **19**, 55–63.
253 F. Göltl, A. M. Love, S. C. Schuenzel, P. Wolf, M. Mavrikakis and I. Hermans, *Phys. Chem. Chem. Phys.*, 2019, **21**, 19065–19075.
254 M. Boronat, C. Martínez-Sánchez, D. Law and A. Corma, *J. Am. Chem. Soc.*, 2008, **130**, 16316–16323.
255 M. Dyballa, *Energy Fuels*, 2023, **37**(23), 18517–18559.
256 J. A. Lercher, C. Grundling and G. Eder-Mirth, *Catal. Today*, 1996, **27**, 353–376.
257 C. J. Wrasman, A. T. Bell, B. D. Chandler, J. W. Harris, S. Kwon, M. R. Ball, S. H. Krishna, S. J. Khatib, P. Bollini, Y. Román-Leshkov, A. "Bean" Getsoian, R. S. Weber, J. A. Lercher, D. Liu, D. E. Resasco, J. S. Bates, J. N. Hall, E. A. Lebrón-Rodríguez, L. Paz Herrera, J. M. Notestein and J. A. Schaidle, *J. Catal.*, 2024, 115451.
258 V. J. Frillette, W. O. Haag and R. M. Lago, *J. Catal.*, 1981, **67**, 218–222.
259 Y. Traa, S. Sealy and J. Weitkamp, in *Characterization II*, ed. H. G. Karge and J. Weitkamp, Springer, Berlin, Heidelberg, 2007, pp. 103–154.
260 M. D. Macedonia and E. J. Maginn, *AIChE J.*, 2000, **46**, 2504–2517.
261 W. O. Haag, R. M. Dessau and R. M. Lago, in *Studies in Surface Science and Catalysis*, ed. T. Lnui, S. Namba and T. Tatsumi, Elsevier, 1991, vol. 60, pp. 255–265.
262 W. O. Haag, R. M. Lago and P. B. Weisz, *Faraday Discuss. Chem. Soc.*, 1981, **72**, 317–330.
263 M. L. Sarazen and E. Iglesia, *J. Catal.*, 2017, **354**, 287–298.
264 J. Van der Mynsbrugge, J. De Ridder, K. Hemelsoet, M. Waroquier and V. Van Speybroeck, *Chem. – Eur. J.*, 2013, **19**, 11568–11576.
265 R. Gounder and E. Iglesia, *Acc. Chem. Res.*, 2012, **45**, 229–238.
266 M. Boudart, *Chem. Rev.*, 1995, **95**, 661–666.
267 C. W. Hullfish, J. Z. Tan, H. I. Adawi and M. L. Sarazen, *ACS Catal.*, 2023, 13140–13150.
268 G. Noh, Z. Shi, S. I. Zones and E. Iglesia, *J. Catal.*, 2018, **368**, 389–410.
269 S. Wang, L. Zhang, S. Li, Z. Qin, D. Shi, S. He, K. Yuan, P. Wang, T.-S. Zhao, S. Fan, M. Dong, J. Li, W. Fan and J. Wang, *J. Catal.*, 2019, **377**, 81–97.
270 S. Wang, P. Wang, Z. Qin, Y. Chen, M. Dong, J. Li, K. Zhang, P. Liu, J. Wang and W. Fan, *ACS Catal.*, 2018, **8**, 5485–5505.
271 T. Liang, J. Chen, Z. Qin, J. Li, P. Wang, S. Wang, G. Wang, M. Dong, W. Fan and J. Wang, *ACS Catal.*, 2016, **6**, 7311–7325.
272 K. Fujimoto, T. Shikada, K. Omata and H. Tominaga, *Chem. Lett.*, 1984, 2047–2050.
273 P. Cheung, E. Iglesia, J. G. Sunley, D. J. Law and A. Bhan, *US Pat.*, US7465822B2, 2008.
274 C. Chizallet, C. Bouchy, K. Larmier and G. Pirngruber, *Chem. Rev.*, 2023, **123**, 6107–6196.
275 P. Cheung, A. Bhan, G. J. Sunley and E. Iglesia, *Angew. Chem., Int. Ed.*, 2006, **45**, 1617–1620.
276 P. Cheung, A. Bhan, G. J. Sunley, D. J. Law and E. Iglesia, *J. Catal.*, 2007, **245**, 110–123.
277 H. Eyring, *J. Chem. Phys.*, 1935, **3**, 107–115.
278 M. G. Evans and M. Polanyi, *Trans. Faraday Soc.*, 1935, **31**, 875–894.
279 M. Boronat, C. Martínez and A. Corma, *Phys. Chem. Chem. Phys.*, 2011, **13**, 2603–2612.
280 D. B. Rasmussen, J. M. Christensen, B. Temel, F. Studt, P. G. Moses, J. Rossmeisl, A. Riisager and A. D. Jensen, *Catal. Sci. Technol.*, 2017, **7**, 1141–1152.
281 Y. Chu, A.-Y. Lo, C. Wang and F. Deng, *J. Phys. Chem. C*, 2019, **123**, 15503–15512.
282 M. Neurock, *Ind. Eng. Chem. Res.*, 2010, **49**, 10183–10199.
283 M. Ešvandtnerová, D. Rocca and T. Bučko, *J. Catal.*, 2021, **396**, 166–178.
284 P. Feng, G. Zhang, X. Chen, K. Zang, X. Li and L. Xu, *Appl. Catal., A.*, 2018, **557**, 119–124.
285 M. Lusardi, T. T. Chen, M. Kale, J. H. Kang, M. Neurock and M. E. Davis, *ACS Catal.*, 2020, **10**, 842–851.
286 J. Yao, Q. Wu, J. Fan, S. Komiyama, X. Yong, W. Zhang, T. Zhao, Z. Guo, G. Yang and N. Tsubaki, *ACS Nano*, 2021, **15**, 13568–13578.
287 X. Feng, J. Yao, H. Li, Y. Fang, Y. Yoneyama, G. Yang and N. Tsubaki, *Chem. Commun.*, 2019, **55**, 1048–1051.
288 Z. Xiong, E. Zhan, M. Li and W. Shen, *Chem. Commun.*, 2020, **56**, 3401–3404.
289 X.-B. Feng, J.-P. Cao, C. Su, Z.-M. He and X.-Y. Zhao, *Fuel*, 2022, **315**, 123267.
290 R. D. Chirico and W. V. Steele, *J. Chem. Eng. Data*, 1997, **42**, 784–790.
291 N. Chakinala and A. G. Chakinala, *Ind. Eng. Chem. Res.*, 2021, **60**, 5331–5351.
292 D. Fraenkel, *Ind. Eng. Chem. Res.*, 1990, **29**, 1814–1821.
293 L. B. Young, S. A. Butter and W. W. Kaeding, *J. Catal.*, 1982, **76**, 418–432.
294 J. Wei, *J. Catal.*, 1982, **76**, 433–439.
295 G. Mirth and J. A. Lercher, *J. Catal.*, 1994, **147**, 199–206.
296 J. E. Leffler, *Science*, 1953, **117**, 340–341.

 This journal is © The Royal Society of Chemistry 2024

Open Access Article. Published on 20 September 2024. Downloaded on 1/24/2026 9:35:52 AM. This article is licensed under a Creative Commons Attribution-NonCommercial 3.0 Unported Licence.

297 G. S. Hammond, *J. Am. Chem. Soc.*, 1955, **77**, 334–338.
298 E. M. Gallego, M. T. Portilla, C. Paris, A. León-Escamilla, M. Boronat, M. Moliner and A. Corma, *Science*, 2017, **355**, 1051–1054.
299 C. Li, C. Paris, J. Martínez-Triguero, M. Boronat, M. Moliner and A. Corma, *Nat. Catal.*, 2018, **1**, 547–554.
300 C. Li, P. Ferri, C. Paris, M. Moliner, M. Boronat and A. Corma, *J. Am. Chem. Soc.*, 2021, **143**, 10718–10726.
301 P. Ferri, C. Li, D. Schwalbe-Koda, M. Xie, M. Moliner, R. Gómez-Bombarelli, M. Boronat and A. Corma, *Nat. Commun.*, 2023, **14**, 2878.
302 M. Moliner and M. Boronat, *Microporous Mesoporous Mater.*, 2023, **358**, 112354.
303 M. Farcasiu and T. F. Degnan, *Ind. Eng. Chem. Res.*, 1988, **27**, 45–47.
304 J. P. Gilson and E. G. Derouane, *J. Catal.*, 1984, **88**, 538–541.
305 J.-Fr Tempere, D. Delafosse and J. P. Contour, *Chem. Phys. Lett.*, 1975, **33**, 95–98.
306 J.-F. R. Tempere, D. Delafosse and J. P. Contour, in *Molecular Sieves—II*, American Chemical Society, 1977, vol. 40, pp. 76–85.
307 R. von Ballmoos and W. M. Meier, *Nature*, 1981, **289**, 782.
308 E. G. Derouane, S. Determmerie, Z. Gabelica and N. Blom, *Appl. Catal.*, 1981, **1**, 201–224.
309 E. G. Derouane, J. P. Gilson, Z. Gabelica, C. Mousty-Desbuquoit and J. Verbist, *J. Catal.*, 1981, **71**, 447–448.
310 A. E. Hughes, K. G. Wilshier, B. A. Sexton and P. Smart, *J. Catal.*, 1983, **80**, 221–227.
311 K. Chao and J. Chern, *Zeolites*, 1988, **8**, 82–85.
312 R. M. Dessau, E. W. Valyocsik and N. H. Goeke, *Zeolites*, 1992, **12**, 776–779.
313 R. Althoff, B. Schulz-Dobrick, F. Schüth and K. Unger, *Microporous Mater.*, 1993, **1**, 207–218.
314 C. S. Cundy, M. S. Henty and R. J. Plaisted, *Zeolites*, 1995, **15**, 342–352.
315 S. A. Schunk, D. G. Demuth, B. Schulz-Dobrick, K. K. Unger and F. Schüth, *Microporous Mater.*, 1996, **6**, 273–285.
316 N. Danilina, F. Krumeich, S. A. Castelanelli and J. A. van Bokhoven, *J. Phys. Chem. C*, 2010, **114**, 6640–6645.
317 J. Shin, N. H. Ahn, S. J. Cho, L. Ren, F.-S. Xiao and S. B. Hong, *Chem. Commun.*, 2014, **50**, 1956–1958.
318 A. Lombard, A. Simon-Masseron, L. Rouleau, A. Cabiac and J. Patarin, *Microporous Mesoporous Mater.*, 2010, **129**, 220–227.
319 Z. Ristanović, J. P. Hofmann, U. Deka, T. U. Schülli, M. Rohnke, A. M. Beale and B. M. Weckhuysen, *Angew. Chem., Int. Ed.*, 2013, **52**, 13382–13386.
320 S. R. Bare, A. Knop-Gericke, D. Teschner, M. Hävacker, R. Blume, T. Rocha, R. Schlögl, A. S. Y. Chan, N. Blackwell, M. E. Charochak, R. ter Veen and H. H. Brongersma, *Surf. Sci.*, 2016, **648**, 376–382.
321 A. Chawla, R. Li, R. Jain, R. John Clark, J. G. Sutjianto, J. C. Palmer and J. D. Rimer, *Mol. Syst. Des. EngMol. Syst. Des. Eng.*, 2018, **3**, 159–170.
322 C. Wang, L. Zhang, X. Huang, Y. Zhu, G. (Kevin) Li, Q. Gu, J. Chen, L. Ma, X. Li, Q. He, J. Xu, Q. Sun, C. Song, M. Peng, J. Sun and D. Ma, *Nat. Commun.*, 2019, **10**, 1–8.
323 T. Li, F. Krumeich, M. Chen, Z. Ma and J. van Bokhoven, *Phys. Chem. Chem. Phys.*, 2020, **22**, 734–739.
324 T. Li, F. Krumeich and J. A. van Bokhoven, *Cryst. Growth Des.*, 2019, **19**(5), 2548–2551.
325 W. Qin, Y. Zhou and J. D. Rimer, *React. Chem. Eng.*, 2019, **4**, 1957–1968.
326 Y. Shen, Z. Qin, S. Asahina, N. Asano, G. Zhang, S. Qian, Y. Ma, Z. Yan, X. Liu and S. Mintova, *J. Mater. Chem. A*, 2021, **9**, 4203–4212.
327 T. T. Le, W. Qin, A. Agarwal, N. Nikolopoulos, D. Fu, M. D. Patton, C. Weiland, S. R. Bare, J. C. Palmer, B. M. Weckhuysen and J. D. Rimer, *Nat. Catal.*, 2023, 1–12.
328 Y. Shen, S. Zhang, Z. Qin, A. Beuque, L. Pinard, S. Asahina, N. Asano, R. Zhang, J. Zhao, Y. Fan, X. Liu, Z. Yan and S. Mintova, *ACS Catal.*, 2024, 3766–3777.
329 F. Jiao, P. Yu, Y. Cui, H. Li, Q. Hu, Y. Xu, S. Mintova, H. Guo and H. Du, *Angew. Chem., Int. Ed.*, 2023, e202310419.
330 L. D. Rollmann, *US Pat.*, US4088605A, 1978.
331 Q. Li, Z. Wang, J. Hedlund, D. Creaser, H. Zhang, X. Zou and A.-J. Bons, *Microporous Mesoporous Mater.*, 2005, **78**, 1–10.
332 D. Van Vu, M. Miyamoto, N. Nishiyama, Y. Egashira and K. Ueyama, *J. Catal.*, 2006, **243**, 389–394.
333 M. Okamoto and Y. Osafune, *Microporous Mesoporous Mater.*, 2011, **143**, 413–418.
334 D. Yi, X. Xu, X. Meng, N. Liu and L. Shi, *J. Porous Mater.*, 2019, **26**, 1767–1779.
335 A. M. Goossens, B. H. Wouters, V. Buschmann and J. A. Martens, *Adv. Mater.*, 1999, **11**, 561–564.
336 Y. Bouizi, I. Diaz, L. Rouleau and V. P. Valtchev, *Adv. Funct. Mater.*, 2005, **15**, 1955–1960.
337 Y. Bouizi, L. Rouleau and V. P. Valtchev, *Chem. Mater.*, 2006, **18**, 4959–4966.
338 G. D. Pirngruber, C. Laroche, M. Maricar-Pichon, L. Rouleau, Y. Bouizi and V. Valtchev, *Microporous Mesoporous Mater.*, 2013, **169**, 212–217.
339 A. Ghorbanpour, A. Gumidyala, L. C. Grabow, S. P. Crossley and J. D. Rimer, *ACS Nano*, 2015, **9**, 4006–4016.
340 S. Han, K. Shilpa, A. J. Mallette, Y. Li, J. B. Hoke and J. D. Rimer, *J. Cryst. Growth*, 2022, 126992.
341 T. T. Le, K. Shilpa, C. Lee, S. Han, C. Weiland, S. R. Bare, P. J. Dauenhauer and J. D. Rimer, *J. Catal.*, 2022, **405**, 664–675.
342 M. Niwa, M. Kato, T. Hattori and Y. Murakami, *J. Phys. Chem.*, 1986, **90**, 6233–6237.
343 T. Hibino, M. Niwa and Y. Murakami, *Zeolites*, 1993, **13**, 518–523.
344 Y. S. Bhat, J. Das, K. V. Rao and A. B. Halgeri, *J. Catal.*, 1996, **159**, 368–374.
345 J.-H. Kim, A. Ishida, M. Okajima and M. Niwa, *J. Catal.*, 1996, **161**, 387–392.
346 C. D. Chang and P. G. Rodewald, *US Pat.*, US5607888A, 1997.
347 S. Zheng, H. R. Heydenrych, A. Jentys and J. A. Lercher, *J. Phys. Chem. B*, 2002, **106**, 9552–9558.
348 S. Zheng, H. R. Heydenrych, H. P. Röger, A. Jentys and J. A. Lercher, *Top. Catal.*, 2003, **22**, 101–106.
349 R. Khare, D. Millar and A. Bhan, *J. Catal.*, 2015, **321**, 23–31.
350 S. Hu, J. Liu, J. Chen, J. Meng, G. Ye and X. Zhou, *Ind. Eng. Chem. Res.*, 2022, **61**, 5747–5756.
351 Y. Wu, J. Han, W. Zhang, Z. Yu, K. Wang, X. Fang, Y. Wei and Z. Liu, *J. Am. Chem. Soc.*, 2024, **146**(12), 8086–8097.
352 A. Corma, V. Fornés, O. Pallota, J. M. Cruz and A. Ayerbe, *J. Chem. Soc., Chem. Commun.*, 1986, **0**, 333–334.
353 G. Garralón, V. Fornés and A. Corma, *Zeolites*, 1988, **8**, 268–272.
354 B. Chauvin, M. Boulet, P. Massiani, F. Fatula, F. Figueras and T. Des Courieres, *J. Catal.*, 1990, **126**, 532–545.
355 Q. L. Wang, M. Torrealba, G. Giannetto, M. Guisnet, G. Perot, M. Cahoreau and J. Caisso, *Zeolites*, 1990, **10**, 703–706.
356 E. Bowes and D. S. Shihabi, *US Pat.*, US5080878A, 1992.
357 E. Benazzi, J. M. Silva, M. F. Ribeiro, F. R. Ribeiro and M. Guisnet, in *Studies in Surface Science and Catalysis*, ed. L. Bonneviot and S. Kaliaguine, Elsevier, 1995, vol. 97, pp. 393–400.
358 J. M. Silva, M. F. Ribeiro, F. R. Ribeiro, N. S. Gnep, M. Guisnet and E. Benazzi, *React. Kinet. Catal. Lett.*, 1995, **54**, 209–215.
359 S. Han, D. S. Shihabi and C. D. Chang, *J. Catal.*, 2000, **196**, 375–378.
360 P. Cañizares and A. Carrero, *Appl. Catal., A.*, 2003, **248**, 227–237.
361 M. R. Apelian, T. F. Degnan and A. S. Fung, *US Pat.*, US5234872A, 1993.
362 H. A. Zaidi and K. K. Pant, *Ind. Eng. Chem. Res.*, 2008, **47**, 2970–2975.
363 J. Lv, Z. Hua, J. Zhou, Z. Liu, H. Guo and J. Shi, *ChemCatChem*, 2018, **10**, 2278–2284.
364 J. Li, L. Wang, D. Zhang, J. Qian, L. Liu and J. Xing, *J. Fuel Chem. Technol.*, 2019, **47**, 957–963.
365 J. Dwyer, F. R. Fitch, F. Machado, G. Qin, S. M. Smyth and J. C. Vickerman, *J. Chem. Soc., Chem. Commun.*, 1981, 422–424.
366 S. Inagaki, S. Shinoda, Y. Kaneko, K. Takechi, R. Komatsu, Y. Tsuboi, H. Yamazaki, J. N. Kondo and Y. Kubota, *ACS Catal.*, 2013, **3**, 74–78.
367 R. Feng, X. Yan, X. Hu, Z. Yan, J. Lin, Z. Li, K. Hou and M. J. Rood, *Catal. Commun.*, 2018, **109**, 1–5.
368 A. Corma, V. Fornés and F. Rey, *Appl. Catal.*, 1990, **59**, 267–274.
369 R. Gounder, A. J. Jones, R. T. Carr and E. Iglesia, *J. Catal.*, 2012, **286**, 214–223.
370 S. Schallmoser, T. Ikuno, M. F. Wagenhofer, R. Kolvenbach, G. L. Haller, M. Sanchez-Sanchez and J. A. Lercher, *J. Catal.*, 2014, **316**, 93–102.
371 K. Lee, S. Lee, Y. Jun and M. Choi, *J. Catal.*, 2017, **347**, 222–230.

Open Access Article. Published on 20 September 2024. Downloaded on 1/24/2026 9:35:52 AM. This article is licensed under a Creative Commons Attribution-NonCommercial 3.0 Unported Licence.

372 M. Abdolrahmani, K. Chen and J. L. White, *J. Phys. Chem. C*, 2018, **122**, 15520–15528.
373 K. Chen, A. Zornes, V. Nguyen, B. Wang, Z. Gan, S. P. Crossley and J. L. White, *J. Am. Chem. Soc.*, 2022, **144**, 16916–16929.
374 S. Namba, A. Inaka and T. Yashima, *Zeolites*, 1986, **6**, 107–110.
375 J. R. Anderson, Y.-F. Chang and R. J. Western, *J. Catal.*, 1989, **118**, 466–482.
376 S. Ezenwa, G. M. Hopping, E. D. Sauer, T. Scott, S. Mack and R. Gounder, *React. Chem. Eng.*, 2024, **9**, 1096–1112.
377 J.-H. Kim, A. Ishida and M. Niwa, *React. Kinet. Catal. Lett.*, 1999, **67**, 281–287.
378 S. Namba, S. Nakanishi and T. Yashima, *J. Catal.*, 1984, **88**, 505–508.
379 T. Yashima, Y. Sakaguchi and S. Namba, in *Studies in Surface Science and Catalysis*, ed. T. Seivama and K. Tanabe, Elsevier, 1981, vol. 7, pp. 739–751.
380 A. Corma, V. Fornés, L. Forni, F. Márquez, J. Martínez-Triguero and D. Moscotti, *J. Catal.*, 1998, **179**, 451–458.
381 X. Zhang, D. Liu, D. Xu, S. Asahina, K. A. Cychosz, K. V. Agrawal, Y. A. Wahedi, A. Bhan, S. A. Hashimi, O. Terasaki, M. Thommes and M. Tsapatsis, *Science*, 2012, **336**, 1684–1687.
382 D. Liu, X. Zhang, A. Bhan and M. Tsapatsis, *Microporous Mesoporous Mater.*, 2014, **200**, 287–290.
383 M. S. Holm, S. Svelle, F. Joensen, P. Beato, C. H. Christensen, S. Bordiga and M. Bjørgen, *Appl. Catal., A*, 2009, **356**, 23–30.
384 C. Freitas, N. S. Barrow and V. Zholobenko, *Johnson. Matthey Technol. Rev.*, 2018, **62**, 279–290.
385 N. M. Page and L. B. Young, *US Pat*., US4855527A, 1989.
386 J. E. Stanat, G. M. K. Mathys, D. W. Turner, J. C. Cheng, S. W. Beadle, C. M. C. Guajardo, R. Eijkhoudt, A. D. Godwin, E. E. Green, C. M. Yarbrough, R. F. Caers, C. B. Duncan and R. Y. Saleh, *US Pat*., US7425662B2, 2008.
387 H. K. Heinichen and W. F. Hölderich, *J. Catal.*, 1999, **185**, 408–414.
388 T. W. Beutel, A. M. Willard, C. Lee, M. S. Martinez and R. Dugan, *J. Phys. Chem. C*, 2021, **125**(16), 8518–8532.
389 A. G. Popov, V. S. Pavlov and I. I. Ivanova, *J. Catal.*, 2016, **335**, 155–164.
390 Y. Zhai, S. Zhang, Y. Shang, Y. Song, W. Wang, T. Ma, L. Zhang, Y. Gong, J. Xu and F. Deng, *Catal. Sci. Technol.*, 2019, **9**, 659–671.
391 Y. Gan, Q. Lv, Y. Li, H. Yang, K. Xu, L. Wu, Y. Tang and L. Tan, *Chem. Eng. Sci.*, 2023, **266**, 118289.
392 L.-Y. Fang, S.-B. Liu and I. Wang, *J. Catal.*, 1999, **185**, 33–42.
393 F. Bauer, W. H. Chen, E. Bilz, A. Freyer, V. Sauerland and S. B. Liu, *J. Catal.*, 2007, **251**, 258–270.
394 M. Molinier and J. S. Abichandani, in *Industrial Arene Chemistry*, John Wiley & Sons, Ltd, 2023, pp. 357–382.
395 M. Molinier, R. G. Tinger, A. Cotte and J. S. Abichandani, in *Industrial Arene Chemistry*, John Wiley & Sons, Ltd, 2023, pp. 327–355.
396 K. Góra-Marek, K. Tarach and M. Choi, *J. Phys. Chem. C*, 2014, **118**, 12266–12274.
397 C. Rieg, Z. Li, A. Kurtz, M. Schmidt, D. Dittmann, M. Benz and M. Dyballa, *J. Phys. Chem. C*, 2021, **125**(1), 515–525.
398 N. S. Nesterenko, F. Thibault-Starzyk, V. Montouilliout, V. V. Yushchenko, C. Fernandez, J.-P. Gilson, F. Fajula and I. I. Ivanova, *Kinet. Catal.*, 2006, **47**, 40–48.
399 D. Fărcaşiu, R. Leu and A. Corma, *J. Phys. Chem. B*, 2002, **106**, 928–932.
400 C. D. Baertsch, K. T. Komala, Y.-H. Chua and E. Iglesia, *J. Catal.*, 2002, **205**, 44–57.
401 B. L. Foley and A. Bhan, *ACS Catal.*, 2020, **10**, 10436–10448.
402 K. M. Keskinen, T. T. Pakkanen, P. Raulo, M. Ruotsalainen, P. Sarv and M. Tutta, in *Studies in Surface Science and Catalysis*, ed. J. Weitkamp, H. G. Karge, H. Pfeifer and W. Hölderich, Elsevier, 1994, vol. 84, pp. 875–882.
403 P. J. Kunkeler, R. S. Downing and H. van Bekkum, *Studies in Surface Science and Catalysis*, Elsevier, 2001, vol. 137, pp. 987–1001.
404 H. P. Röger, K. P. Möller, W. Böhringer and C. T. O'Connor, *Studies in Surface Science and Catalysis*, Elsevier, 2000, vol. 130, pp. 2909–2914.
405 C. Li, H. J. Cho, Z. Wang, J. Gou, Y. Ren, H. Xi and W. Fan, *ChemCatChem*, 2016, **8**, 2406–2414.
406 A. Korde, B. Min, Q. Almas, Y. Chiang, S. Nair and C. W. Jones, *ChemCatChem*, 2019, **11**, 4548–4557.
407 L. Emdadi, S. C. Oh, Y. Wu, S. N. Oliaee, Y. Diao, G. Zhu and D. Liu, *J. Catal.*, 2016, **335**, 165–174.
408 H. I. Adawi, F. O. Odigie and M. L. Sarazen, *Mol. Syst. Des. Eng.*, 2021, **6**, 903–917.
409 D. Xu, O. Abdelrahman, S. H. Ahn, Y. Guefrachi, A. Kuznetsov, L. Ren, S. Hwang, M. Khaleel, S. Al Hassan, D. Liu, S. B. Hong, P. Dauenhauer and M. Tsapatsis, *AIChE J.*, 2019, **65**, 1067–1075.
410 K. Hashimoto, T. Masuda and Y. Hariguchi, *Nippon Kagaku Kaishi*, 1989, **3**, 575–582.
411 D. Fraenkel, *J. Catal.*, 1989, **118**, 10–21.
412 A. W. Burton and S. I. Zones, in *Studies in Surface Science and Catalysis*, ed. J. Čejka, H. van Bekkum, A. Corma and F. Schüth, Elsevier, 2007, vol. 168, pp. 137–179.
413 T. Ikuno, W. Chaikittisilp, Z. Liu, T. Iida, Y. Yanaba, T. Yoshikawa, S. Kohara, T. Wakihara and T. Okubo, *J. Am. Chem. Soc.*, 2015, **137**, 14533–14544.
414 J. E. Schmidt, D. Fu, M. W. Deem and B. M. Weckhuysen, *Angew. Chem., Int. Ed.*, 2016, **55**, 16044–16048.
415 S. Li, R. Gounder, A. Debellis, I. B. Müller, S. Prasad, A. Moini and W. F. Schneider, *J. Phys. Chem. C*, 2019, **123**, 17454–17458.
416 M. Kumar, Z. J. Berkson, R. J. Clark, Y. Shen, N. A. Prisco, Q. Zheng, Z. Zeng, H. Zheng, L. B. McCusker, J. C. Palmer, B. F. Chmelka and J. D. Rimer, *J. Am. Chem. Soc.*, 2019, **141**, 20155–20165.
417 Q. Ke, I. Khalil, B. Smeyers, Z. Li, R. de Oliveira-Silva, B. Sels, D. Sakellariou and M. Dusselier, *Angew. Chem., Int. Ed.*, 2021, **60**, 24189–24197.
418 S. I. Zones, K. Jayanthi, J. Pascual, D. Xie and A. Navrotsky, *Chem. Mater.*, 2021, **33**, 2126–2138.
419 D. Schwalbe-Koda, S. Kwon, C. Paris, E. Bello-Jurado, Z. Jensen, E. Olivetti, T. Willhammar, A. Corma, Y. Román-Leshkov, M. Moliner and R. Gómez-Bombarelli, *Science*, 2021, **374**, 308–315.
420 C. Waitt, X. Gao, R. Gounder, A. Debellis, S. Prasad, A. Moini and W. F. Schneider, *J. Phys. Chem. C*, 2023, **127**(46), 22740–22751.
421 F. Daeyaert and M. Deem, *AI-Guided Design and Property Prediction for Zeolites and Nanoporous Materials*, John Wiley & Sons, Ltd, 2023, pp. 33–59.
422 C. M. Lew, D. Xie, J. E. Schmidt, S. Elomari, T. M. Davis and S. I. Zones, *AI-Guided Design and Property Prediction for Zeolites and Nanoporous Materials*, John Wiley & Sons, Ltd, 2023, pp. 1–32.
423 J. Shin, N. H. Ahn, M. A. Camblor, S. J. Cho and S. B. Hong, *Angew. Chem., Int. Ed.*, 2014, **53**, 8949–8952.
424 J. Shin, N. H. Ahn, M. A. Camblor, C. M. Zicovich-Wilson and S. B. Hong, *Chem. Mater.*, 2014, **26**, 3361–3363.
425 J. Devos, S. Robijns, C. Van Goethem, I. Khalil and M. Dusselier, *Chem. Mater.*, 2021, **33**, 2516–2531.
426 S. Lee, C. T. Nimlos, E. R. Kipp, Y. Wang, X. Gao, W. F. Schneider, M. Lusardi, V. Vattipalli, S. Prasad, A. Moini and R. Gounder, *Cryst. Growth Des.*, 2022, **22**(10), 6275–6295.
427 H. I. Adawi, Y. Zheng and M. L. Sarazen, *Cryst. Growth Des.*, 2023, **23**, 2675–2688.
428 J. A. van Bokhoven, D. C. Koningsberger, P. Kunkeler, H. van Bekkum and A. P. M. Kentgens, *J. Am. Chem. Soc.*, 2000, **122**, 12842–12847.
429 T. Jarrin, T. de Bruin and C. Chizallet, *ACS Catal.*, 2024, 1639–1652.
430 C. Lei, A. Erlebach, F. Brivio, L. Grajciar, Z. Tošner, C. J. Heard and P. Nachtigall, *Chem. Sci.*, 2023, **14**, 9101–9113.
431 J. Martinez-Ortigosa, J. Simancas, J. A. Vidal-Moya, P. Gaveau, F. Rey, B. Alonso and T. Blasco, *J. Phys. Chem. C*, 2019, **123**, 22324–22334.
432 H. Xiong, Z. Liu, X. Chen, H. Wang, W. Qian, C. Zhang, A. Zheng and F. Wei, *Science*, 2022, **376**, 491–496.
433 B. Shen, H. Wang, H. Xiong, X. Chen, E. G. T. Bosch, I. Lazić, W. Qian and F. Wei, *Nature*, 2022, 1–5.
434 B. Shen, X. Chen, H. Wang, H. Xiong, E. G. T. Bosch, I. Lazić, D. Cai, W. Qian, S. Jin, X. Liu, Y. Han and F. Wei, *Nature*, 2021, **592**, 541–544.
435 H. Xiong, H. Wang, X. Chen and F. Wei, *ACS Catal.*, 2023, **13**, 12213–12226.
436 A. Hwang, T. T. Le, Z. Shi, H. Dai, J. D. Rimer and A. Bhan, *J. Catal.*, 2019, **369**, 122–132.
437 B. L. Foley, B. A. Johnson and A. Bhan, *ACS Catal.*, 2021, 3628–3637.
438 N. K. Razdan, A. Kumar and A. Bhan, *J. Catal.*, 2019, **372**, 370–381.
439 Y. G. Hur, P. M. Kester, C. T. Nimlos, Y. Cho, J. T. Miller and R. Gounder, *Ind. Eng. Chem. Res.*, 2019, **58**, 11849–11860.

 This journal is © The Royal Society of Chemistry 2024

Open Access Article. Published on 20 September 2024. Downloaded on 1/24/2026 9:35:52 AM.
This article is licensed under a Creative Commons Attribution-NonCommercial 3.0 Unported Licence.

440 R. Kolvenbach, N. Al-Yassir, S. S. Al-Khattaf, O. C. Gobin, J. H. Ahn, A. Jentys and J. A. Lercher, *Catal. Today*, 2011, **168**, 147–157.
441 T. Masuda, *Catal. Surv. Asia*, 2003, **7**, 133–144.
442 R. Davis, *AIChE J.*, 2018, **64**, 3778–3785.
443 A. Bhan and W. N. Delgass, *J. Catal.*, 2022, **405**, 419–429.
444 C. D. Chang and A. J. Silvestri, *J. Catal.*, 1977, **47**, 249–259.
445 R. J. Quann, L. A. Green, S. A. Tabak and F. J. Krambeck, *Ind. Eng. Chem. Res.*, 1988, **27**, 565–570.
446 S. Ilias and A. Bhan, *ACS Catal.*, 2013, **3**, 18–31.
447 M. Moliner, J. M. Serra, A. Corma, E. Argente, S. Valero and V. Botti, *Microporous Mesoporous Mater.*, 2005, **78**, 73–81.
448 A. Corma, M. J. Díaz-Cabañas, J. L. Jordá, C. Martínez and M. Moliner, *Nature*, 2006, **443**, 842–845.
449 A. Corma, M. Moliner, J. M. Serra, P. Serna, M. J. Díaz-Cabañas and L. A. Baumes, *Chem. Mater.*, 2006, **18**, 3287–3296.
450 R. Pophale, P. A. Cheeseman and M. W. Deem, *Phys. Chem. Chem. Phys.*, 2011, **13**, 12407–12412.
451 K. Muraoka, Y. Sada, D. Miyazaki, W. Chaikittisilp and T. Okubo, *Nat. Commun.*, 2019, **10**, 4459.
452 E. Pan, S. Kwon, Z. Jensen, M. Xie, R. Gómez-Bombarelli, M. Moliner, Y. Román-Leshkov and E. Olivetti, *ACS Cent. Sci.*, 2024, **10**(3), 729–743.
453 Z. Jensen, E. Kim, S. Kwon, T. Z. H. Gani, Y. Román-Leshkov, M. Moliner, A. Corma and E. Olivetti, *ACS Cent. Sci.*, 2019, **5**(5), 892–899.
454 Z. Jensen, S. Kwon, D. Schwalbe-Koda, C. Paris, R. Gómez-Bombarelli, Y. Román-Leshkov, A. Corma, M. Moliner and E. A. Olivetti, *ACS Cent. Sci.*, 2021, **7**(5), 858–867.
455 K. Muraoka, W. Chaikittisilp and T. Okubo, *Chem. Sci.*, 2020, **11**, 8214–8223.
456 M. Moliner, Y. Román-Leshkov and A. Corma, *Acc. Chem. Res.*, 2019, **52**, 2971–2980.
457 J. Sauer, *J. Catal.*, 2024, **433**, 115482.
458 J. O. Hirschfelder, C. F. Curtiss and R. B. Bird, *The Molecular Theory of Gases and Liquids*, Wiley-Interscience, Hoboken, NJ, Revised edn, 1964.
459 D. W. Breck, *Zeolite Molecular Sieves: Structure, Chemistry, and Use*, Wiley, 1973.
460 C. E. Webster, R. S. Drago and M. C. Zerner, *J. Am. Chem. Soc.*, 1998, **120**, 5509–5516.
461 V. R. Choudhary, V. S. Nayak and T. V. Choudhary, *Ind. Eng. Chem. Res.*, 1997, **36**, 1812–1818.
462 M. L. Connolly, *Science*, 1983, **221**, 709–713.
463 S. Herrmann and E. Iglesia, *J. Catal.*, 2017, **346**, 134–153.